Back-arc extension in the Andaman Sea: Tectonic and magmatic processes imaged by high-precision teleseismic double-difference earthquake relocation

T. Diehl,[1,2] F. Waldhauser,[1] J. R. Cochran,[1] K. A. Kamesh Raju,[3] L. Seeber,[1] D. Schaff,[1] and E. R. Engdahl[4]

Received 10 August 2012; revised 29 March 2013; accepted 16 April 2013; published 15 May 2013.

[1] The geometry, kinematics, and mode of back-arc extension along the Andaman Sea plate boundary are refined using a new set of significantly improved hypocenters, global centroid moment tensor (CMT) solutions, and high-resolution bathymetry. By applying cross-correlation and double-difference (DD) algorithms to regional and teleseismic waveforms and arrival times from International Seismological Centre and National Earthquake Information Center bulletins (1964–2009), we resolve the fine-scale structure and spatiotemporal behavior of active faults in the Andaman Sea. The new data reveal that back-arc extension is primarily accommodated at the Andaman Back-Arc Spreading Center (ABSC) at ~10°, which hosted three major earthquake swarms in 1984, 2006, and 2009. Short-term spreading rates estimated from extensional moment tensors account for less than 10% of the long-term 3.0–3.8 cm/yr spreading rate, indicating that spreading by intrusion and the formation of new crust make up for the difference. A spatiotemporal analysis of the swarms and Coulomb-stress modeling show that dike intrusions are the primary driver for brittle failure in the ABSC. While spreading direction is close to ridge normal, it is oblique to the adjacent transforms. The resulting component of E-W extension across the transforms is expressed by deep basins on either side of the rift and a change to extensional faulting along the West Andaman fault system after the $Mw = 9.2$ Sumatra-Andaman earthquake of 2004. A possible skew in slip vectors of earthquakes in the eastern part of the ABSC indicates an en-echelon arrangement of extensional structures, suggesting that the present segment geometry is not in equilibrium with current plate-motion demands, and thus the ridge experiences ongoing re-adjustment.

Citation: Diehl, T., F. Waldhauser, J. R. Cochran, K. A. Kamesh Raju, L. Seeber, D. Schaff, and E. R. Engdahl (2013), Back-arc extension in the Andaman Sea: Tectonic and magmatic processes imaged by high-precision teleseismic double-difference earthquake relocation, *J. Geophys. Res. Solid Earth*, *118*, 2206–2224, doi:10.1002/jgrb.50192.

1. Introduction

[2] The Andaman Sea in the northeast Indian Ocean is an actively opening marginal basin inboard of the Western Sunda Arc (Figure 1). Extension in the Andaman Sea is primarily driven by oblique subduction of the Indian-Australian plate beneath the western Sunda arc, in contrast to back-arc basins in the southwestern Pacific, where extension is mainly associated with trench rollback [e.g., *Uyeda and Kanamori*, 1979]. Oblique plate convergence is accommodated in part by strain partitioning along this subduction zone resulting in arc-parallel strike-slip faulting and the formation of a northward moving sliver plate [e.g., *Fitch*, 1972; *McCaffrey*, 1992; *McCaffrey*, 2009]. The boundary between the sliver, Burma Plate, and the Sunda Plate is a system of arc-parallel transforms and arc-normal ridges in the back-arc of the Andaman Sea, which connects to the right-lateral Sumatra fault along the volcanic arc in the southwest (Figure 1). The connection with the Sagaing Fault to the northeast is less distinct, and different geometries have been proposed [e.g., *Rangin et al.*, 1999; *Curray*, 2005] (see Figure 1). As the Burma Plate is dragged northward (with respect to the Sunda Plate) by the underthrusting Indian-Australian plate, "pull-apart" basins develop along the plate boundary, resulting in NE-SW extension of the Andaman Sea [e.g., *Curray*, 2005; *McCaffrey*, 2009]. While the term "pull-apart" usually refers to intracrustal extension along a strike-slip system, extension in the Andaman Sea involves the formation of new crust

Additional supporting information may be found in the online version of this article.

[1]Lamont-Doherty Earth Observatory, Columbia University, Palisades, New York, USA.
[2]Now at Swiss Seismological Service, ETH Zurich, Zurich, Switzerland.
[3]National Institute of Oceanography, Dona Paula, Goa, India.
[4]Department of Physics, University of Colorado, Boulder, Colorado, USA.

Corresponding author: T. Diehl, Swiss Seismological Service, ETH Zurich, Sonneggstrasse 5, CH-8092, Zurich, Switzerland. (tobias.diehl@sed.ethz.ch)

2169-9313/13/10.1002/jgrb.50192

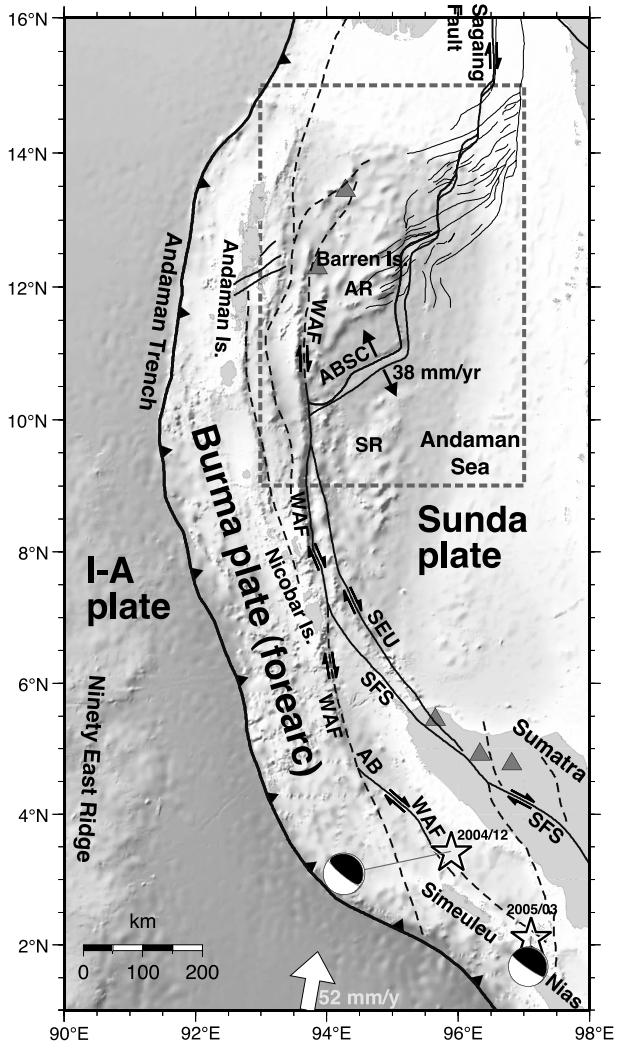

Figure 1. Simplified tectonic map of the Sumatra-Andaman region with active faults indicated by solid lines and inactive faults marked as dashed black lines [after *Curray*, 2005]. Thin lines indicate the extensional horsetail system forming the southern termination of the Sagaing Fault as proposed by *Rangin et al*. [1999]. Dashed box indicates study area. Convergence rate is from *Sieh and Natawidjaja* [2000], spreading rate in the Andaman Sea is from *Kamesh Raju et al*. [2004]. Stars correspond to NEIC epicenters of the December 2004 Sumatra-Andaman and March 2005 Nias events. Corresponding global CMT solutions are plotted at their centroid locations. Triangles correspond to volcanic arc [*Siebert and Simkin*, 2002]. Bold labels indicate plates. AB: Aceh Basin, ABSC: Andaman Back-Arc Spreading Center, AR: Alcock Rise, I-A: Indian-Australian, SEU: Seulimeum strand of the Sumatra fault system, SFS: Sumatra fault system, SR: Sewell Rise, WAF: West Andaman fault.

[*Kamesh Raju et al*., 2004] and justifies identifying the sliver as a distinct plate. This transtensional mode of back-arc opening is also referred to as "rhombochasm" [e.g., *Rodolfo*, 1969; *Curray*, 2005] or "leaky-transform" [e.g., *Thompson and Melson*, 1972; *Uyeda and Kanamori*, 1979; *Taylor et al*., 1994].

[3] The first geophysical evidence for active opening of the Andaman Sea was derived from bathymetric, magnetic, gravimetric, heat flow, and seismic surveys [e.g., *Rodolfo*, 1969; *Curray et al*., 1979; for a summary, see *Curray*, 2005]. *Kamesh Raju et al*. [2004] mapped the structure of the Andaman Back-Arc Spreading Center (ABSC, Figure 1) in detail, using high-resolution multibeam swath bathymetry in combination with magnetic and single-channel seismic surveys. They identify three SW-NE trending spreading segments, separated by left-stepping offsets of several kilometers. Interpretation of magnetic anomalies suggests that true seafloor spreading started at about 4 Ma and is thus much younger than the Sunda arc. It may still be developing, according to the kinematic model of *Kamesh Raju et al*. [2004] that implies a westward propagation of the spreading center. Magnetic anomalies suggest an initial spreading rate of 1.6 cm/yr and an increase in rate up to 3.8 cm/yr from about 2–2.5 Ma to present [*Kamesh Raju et al*., 2004]. The estimated 118 km opening of the ABSC over 4 Myr results in an average rate of 3.0 cm/yr [*Curray*, 2005]. *Chamot-Rooke et al*. [2001] proposed a similar range of spreading rate of 2.8–3.6 cm/yr. With a present full rate in the range of 3.0–3.8 cm/yr, the Andaman Spreading Center is in the class of slow-spreading ridges [e.g., *Dick et al*., 2003].

[4] Early evidence for neotectonic extension was based on focal mechanisms determined from teleseismic records of earthquakes in the Andaman Sea. *Fitch* [1972] found three normal-faulting events in the northern part of the Andaman Sea, indicating a WNW-NW extension. In addition, he associated four right-lateral strike-slip events located north and northwest of Sumatra with a submarine continuation of the Sumatra fault system. The existence of two spreading centers located at 10°N and at 14°N separated by a N-S transform fault was inferred from the recovery of additional right-lateral strike-slip and normal-faulting mechanisms in the Andaman Sea by *Eguchi et al*. [1979]. *Guzmán-Speziale and Ni* [1993] obtained the strikingly low short-term spreading velocity of 0.05 cm/yr in the Andaman Sea from summing seismic moment tensors of normal-faulting events between 1964 and 1986, much smaller than the calculated displacement velocity along the right-lateral Sagaing Fault. Their spreading velocity was based on the assumption of full coupling in a deeply rooted extension regime with no contribution from magmatic injection and is likely an underestimate.

[5] Earthquakes in the Andaman Sea often occur clustered in space and time as noted, e.g., in *Mukhopadhyay and Dasgupta* [2008] and shown in Figure S1 in the supporting information. In the course of this study, we use the term "cluster" to indicate spatial clustering and "sequence" for spatial as well as temporal clustering of earthquakes. Special types of sequences are "swarms," which typically lack a distinct main shock, show an unusually large spatial extent compared to the moment release of the largest individual event, and have magnitudes that fail to decay with time [e.g., *Roland and McGuire*, 2009]. The characteristics of several earthquake sequences in the Andaman Sea are described in detail in section S.1 of the supporting information. Earthquake swarms were observed in 1973, 1983–1984, and 1993, particularly in the south Andaman Sea (Figures 2, S1, and S2). In March 2006, more than 1 year after the $Mw = 9.2$ December 2004 Sumatra-Andaman earthquake, an earthquake swarm

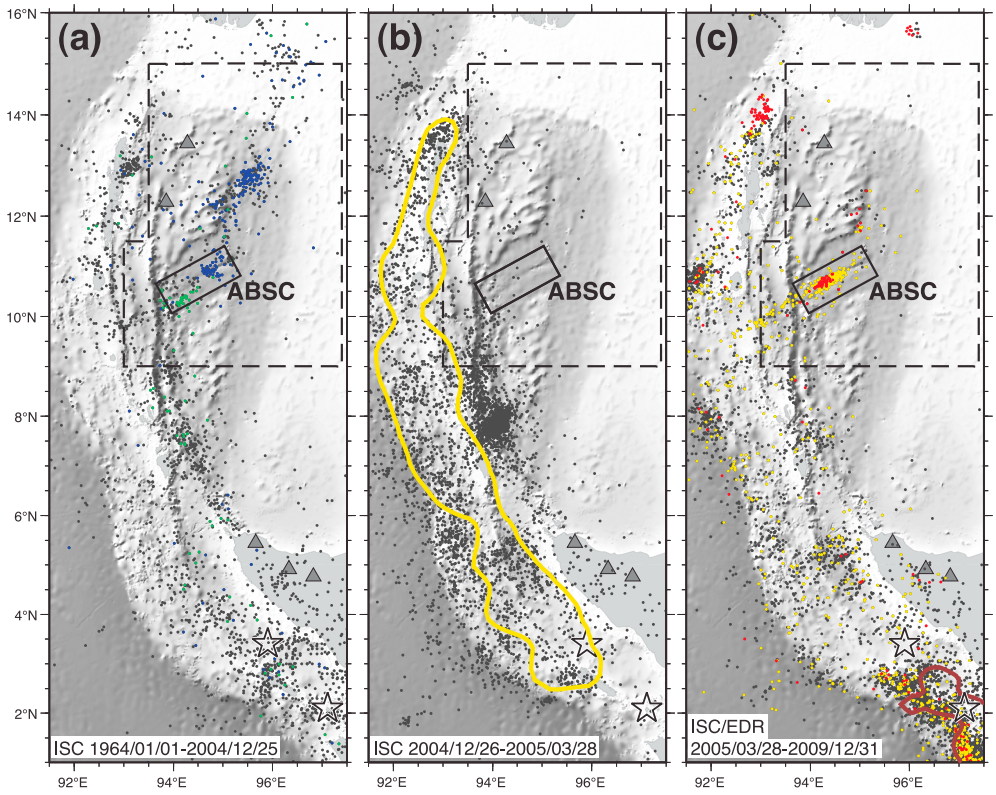

Figure 2. Seismicity in the Sumatra-Andaman region as reported in the ISC and EDR bulletins for focal depths ≤40 km. (a) Time period: 1 January 1964 to 25 December 2004. Blue dots correspond to events between 1983 and 1984; green dots indicate events between 1993 and 1994. Stars indicate epicenters of the 2004 Sumatra-Andaman earthquake and 2005 Nias earthquake. Dashed line indicates outline of back-arc region studied. (b) Time period: 26 December 2004 ($Mw = 9.2$ Sumatra-Andaman earthquake) to 28 March 2005. Yellow line indicates rupture area of the 2004 Sumatra-Andaman earthquake based on the slip model of *Chlieh et al.* [2007]. (c) Time period: 28 March 2005 ($Mw = 8.7$ Nias earthquake) to end of 2009. Yellow dots correspond to events in 2006; red dots indicate events in 2009. Brown line indicates rupture area of the 2005 Nias earthquake based on the slip model of *Briggs et al.* [2006].

occurred in the ABSC, followed by another swarm in July 2009 (Figures 2, S1, and S2). The swarm-like occurrence of earthquakes is indicative of episodic rifting events. Major earthquake swarms in the ABSC appear to occur roughly every 10 years, with the exception of the 2009 swarm, which occurred after a quiescence of only 3 years (Figure S1).

[6] Existing models of plate-boundary structure and tectonic processes in the Andaman Sea are based in large part on global bulletin earthquake locations and associated focal mechanisms. Bulletin locations such as provided by the ISC (International Seismological Centre) or EDR (Earthquake Data Report of the National Earthquake Information Center, NEIC) typically have spatial resolution (depth in particular) below the scale length of tectonic structures in this region and hamper seismotectonic interpretations. To better understand the underlying mechanisms of the earthquake swarms in the Andaman Sea, we use cross-correlation and double-difference methods to significantly improve the hypocenter locations in standard global earthquake catalogs. The high-resolution time-space seismicity patterns together with global centroid moment tensor (CMT) solutions starting in 1976 (http://www.globalcmt.org) and detailed seafloor bathymetry are combined to construct and discuss an improved seismotectonic framework for the Andaman Back-Arc region.

2. Data and Double-Difference Relocation

[7] We use phase arrival time data observed at regional and global seismic networks and published in the ISC bulletin for the years 1964–2006 and in the EDR bulletin for the years 2007–2009, as well as digital waveform data obtained from the Incorporated Research Institutions for Seismology (IRIS). The combined ISC/EDR catalog includes a total of 19,000 earthquakes in the Sumatra-Andaman region, 1266 of which occurred in the Andaman Sea (area outlined by dashed line in Figure 2) and are discussed in this paper. The hypocenters in these catalogs are estimated using single-event location methods that invert arrival times for the absolute location of the hypocenter and its origin time. Due to limited station coverage, inconsistencies in phase association, uncertainties in arrival time readings, and errors in the model used to predict the data, the spatial resolution of these locations is often low. Because of the trade-off between origin time and depth for events recorded at teleseismic distances, focal depths are often unconstrained and set to a default value.

[8] Previous relocation studies include *Engdahl et al.* [2007], who relocated a subset of the global bulletin data for the Sumatra-Andaman region following the Engdahl-van der

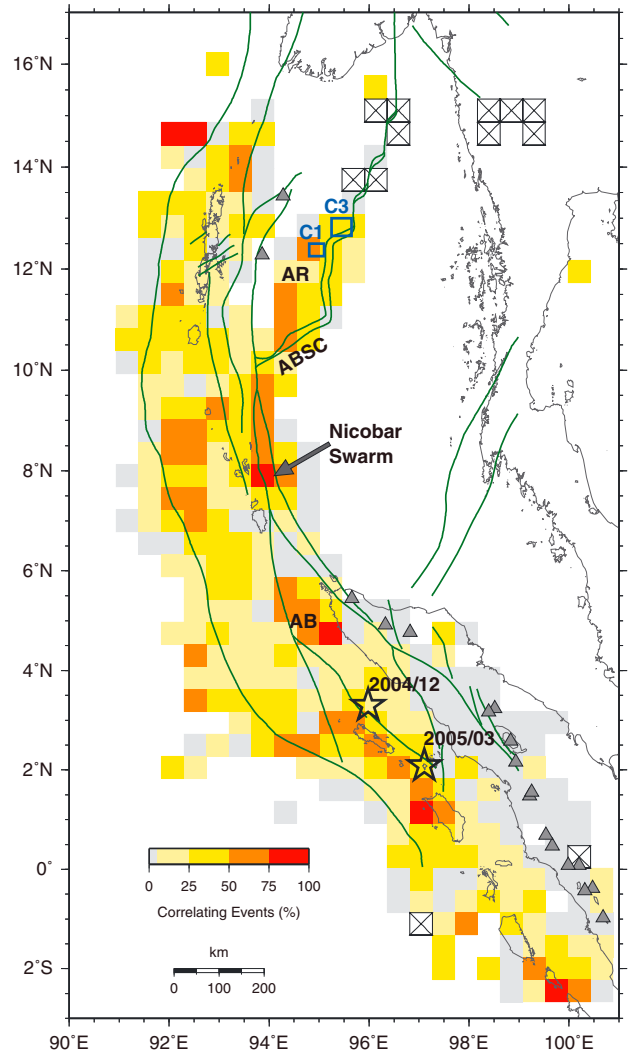

Figure 3. Percentage of correlated events within volumes of 50 × 50 × 50 km between 0 and 50 km depth. Correlated events in the map are defined to have at least four correlation measurements with cross-correlation coefficients ≥0.8 over less than 50 km hypocenter separation. Volumes with less than five events and events with less than four waveforms are not included. Crosses indicate volumes with more than five events but with no waveform data available. Epicenters of $Mw = 9.2$ and $Mw = 8.7$ earthquakes are indicated by stars. Green lines indicate tectonic features [after *Curray*, 2005]. Triangles denote volcanic arc [*Siebert and Simkin*, 2002]. Blue boxes include clusters C1 and C3 shown in Figure 4. AB: Aceh Basin, ABSC: Andaman Back-Arc Spreading Center, AR: Alcock Rise.

Hilst-Buland (EHB) procedure, which computes a groomed catalog of the highest-quality events with improved depths by using depth phases obtained by probabilistic phase association [*Engdahl et al.*, 1998]. *Pesicek et al.* [2010] relocated the EHB catalog by applying a double-difference algorithm to first arriving *P* waves and depth phases extracted from the EHB bulletin and measured via waveform cross-correlation together with a regional 3-D velocity model.

[9] In this study, we aim to resolve and study in a comprehensive way the fine details of active faulting in the Andaman Sea by applying the teleseismic double-difference (hypoDD) algorithm of *Waldhauser and Schaff* [2007] to all first and later arriving *P* and *S* phase data reported in the ISC and EDR bulletins. The double-difference method removes unmodeled velocity structure by directly inverting travel-time differences between events for their hypocenter separation [*Waldhauser and Ellsworth*, 2000]. This approach permits the combined use of phase delay times measured from bulletin picks and from cross-correlation of similar seismograms. Cross-correlation (CC) methods can measure differential phase arrival times with subsample precision for events that are nearby and have similar focal mechanisms, typically resulting in more than an order of magnitude improvement over delay times formed from phase onset picks reported in earthquake bulletins [*Poupinet et al.*, 1984; *Waldhauser and Schaff et al.*, 2007].

2.1. Waveform Cross-Correlation

[10] While the following cross-correlation results pertain to the entire Sumatra-Andaman region, their subsequent analysis and interpretation focuses on the Andaman Sea. We extracted 7 million waveforms of more than 19,000 events from the IRIS and GEOFON data centers, selecting the best ~1000 regional and global stations from the Global Seismic Network, the GEOFON network (http://geofon.gfz-potsdam.de), and the GEOSCOPE network (http://geoscope.ipgp.fr). All available stations within a radius of 30° from the Sumatra-Andaman region and all available stations in the Southern Hemisphere were used. Typically less than 10 records are available for events that occurred prior to 1990 and none for events before 1984. We perform time-domain cross-correlation [*Schaff et al.*, 2004; *Waldhauser and Schaff*, 2007] on 9 s long windows around the predicted first arriving *P* and *S* phases. Waveforms of all pairs of events separated by less than 300 km are cross-correlated. A band-pass filter of 0.5 to 2.0 Hz is applied to seismograms prior to cross-correlation in order to increase the signal-to-noise ratio of the body waves.

[11] The distribution of the CC measurements across the Sumatra-Andaman region is shown in Figure 3. Colors indicate percentage of correlating events within bins of 50 × 50 × 50 km. We exclude deeper events in Figure 3 to show the correlation results for crustal events in the back-arc discussed later. We define a correlated event as event that has at least four CC measurements with correlation coefficients ≥0.8 with at least one neighboring event. High numbers of correlating events occur updip of the nucleation of the 2004 Sumatra-Andaman and 2005 Nias megathrust earthquakes, beneath the Aceh Basin (AB, Figure 3), in the region of the January 2005 Nicobar-Swarm [e.g., *Kundu et al.*, 2012], along the Andaman Spreading Center, and at the NE edge of the Alcock Rise (AR, Figure 3). We associate these patches of high correlation as regions of increased earthquake density where earthquakes appear to rupture the same faults with similar slip orientations. Beneath the Aceh Basin, for example, such repeated slip occurs on the megathrust and on imbricate faults in the mantle wedge [*Waldhauser et al.*, 2012]. Low numbers of correlating events occur along the volcanic arc and the Sumatra fault system (Figure 3), which is likely due to the complex and highly segmented fault structures on-shore northern Sumatra [*Sieh and Natawidjaja*, 2000].

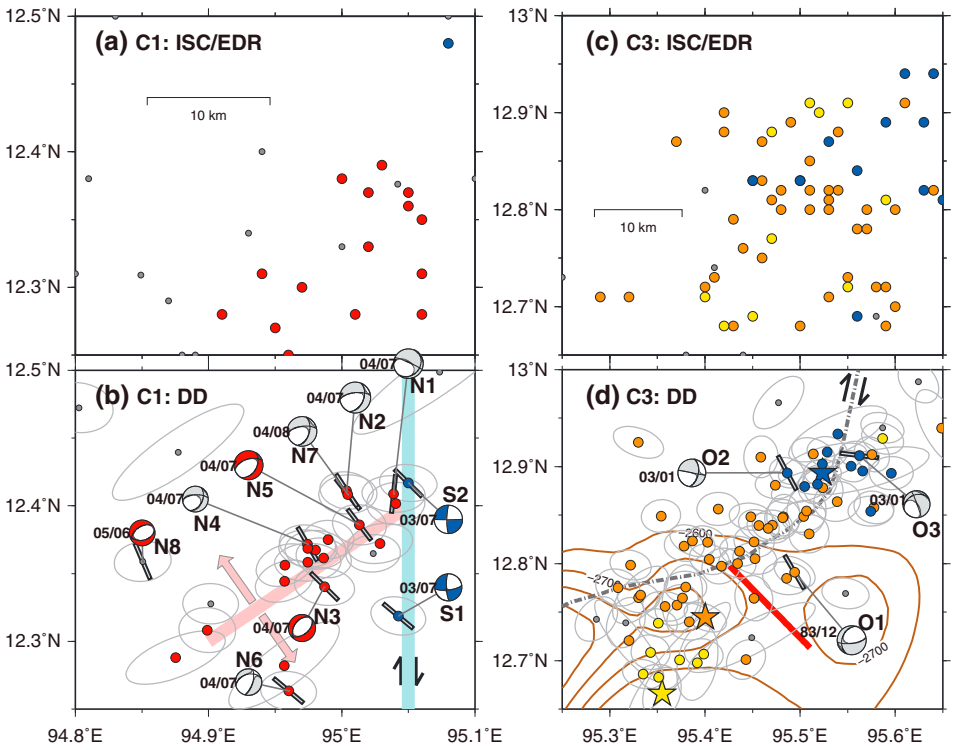

Figure 4. (a, b) Comparison of ISC/EDR bulletin locations (top row) with DD results (bottom row) for seismicity cluster C1 (see blue box in Figure 3 for location). Blue dots: July 2003; red: July to August 2004. Bold pink line indicates strike of normal fault inferred from cluster orientation and CMT solutions. Bold blue line indicates strike of adjacent transform fault inferred from CMT solutions and bathymetry. (c, d) Comparison of ISC/EDR bulletin locations (top row) with DD results (bottom row) for seismicity cluster C3 (see blue box in Figure 3 for location). Orange dots: December 1983; yellow: January 1984; blue: January 2003. Stars indicate initiation of sequences. The red line marks the width of the rift valley identified by *Curray* [2005] along the NW-SE oriented seismic reflection profile I 19–20. Contour lines correspond to satellite bathymetry between −2900 and −2600 m; gray dash-dotted line indicates notional plate boundary. Global CMT solutions in Figures 4b and 4d are color coded by type of faulting: red = normal fault (plunge of *P* axis ≥60°, plunge of *B* and *T* axes ≤45°); blue = strike slip (plunge of *B* axis ≥60°, plunge of *P* and *T* axes ≤45°); gray = oblique slip (mechanisms which fall outside normal-fault and strike-slip definitions). Black lines on the beach-ball symbols indicate nodal planes of the double-couple part of the moment tensor. Bars correspond to orientation of *T* axes from CMT solutions. Label left of beach-ball symbols denotes year/month of event. Gray ellipses indicate the 90% confidence interval of relative locations derived from bootstrap analysis.

2.2. Teleseismic Multiphase Double-Difference Relocation

[12] We combine 40,000 high-precision correlation delay-time measurements for events within the back-arc region with 1.3 million delay times formed from bulletin picks and invert the data for relative hypocenter locations using the teleseismic hypoDD algorithm of *Waldhauser and Schaff* [2007]. In order to reduce the number of outliers caused by cycle skipping in the correlation data, only CC measurements with CC coefficient ≥0.8 are used. We compute pick delay times from all first and later arriving *P* and *S* phase data listed in the ISC/EDR bulletins. The use of core phases with their steep takeoff angles, in addition to depth phases, is especially important to constrain relative depths. The global travel-time model ak135 is used to predict the observed data. To reduce the impact of the inhomogeneous station distribution, we selected for each event pair independently the best station within bins of 3° across the globe before relocation (see *Waldhauser and Schaff* [2007] for details).

[13] To reduce the often significant errors in the ISC and EDR bulletin locations, which can lead to an incomplete network of delay time links, we relocate each event listed in these catalogs individually relative to events in an updated (1918–2009) and DD relocated version of the EHB catalog for the Sumatra-Andaman region [*Engdahl et al.*, 2007] using a single-event DD algorithm [*Waldhauser*, 2009; *Waldhauser et al.*, 2012]. The improved single-event DD locations are subsequently used to generate a new network of phase delay times from the combined ISC and EDR bulletins and are taken as starting locations for a final simultaneous inversion of both correlation and phase pick delay time data. The final DD relocations have an RMS of 0.72 s for bulletin pick data. The RMS value for correlation data is on the order of 60 ms for earthquakes with well-correlated seismograms, such as observed in cluster C1 (Figures 3 and 4b).

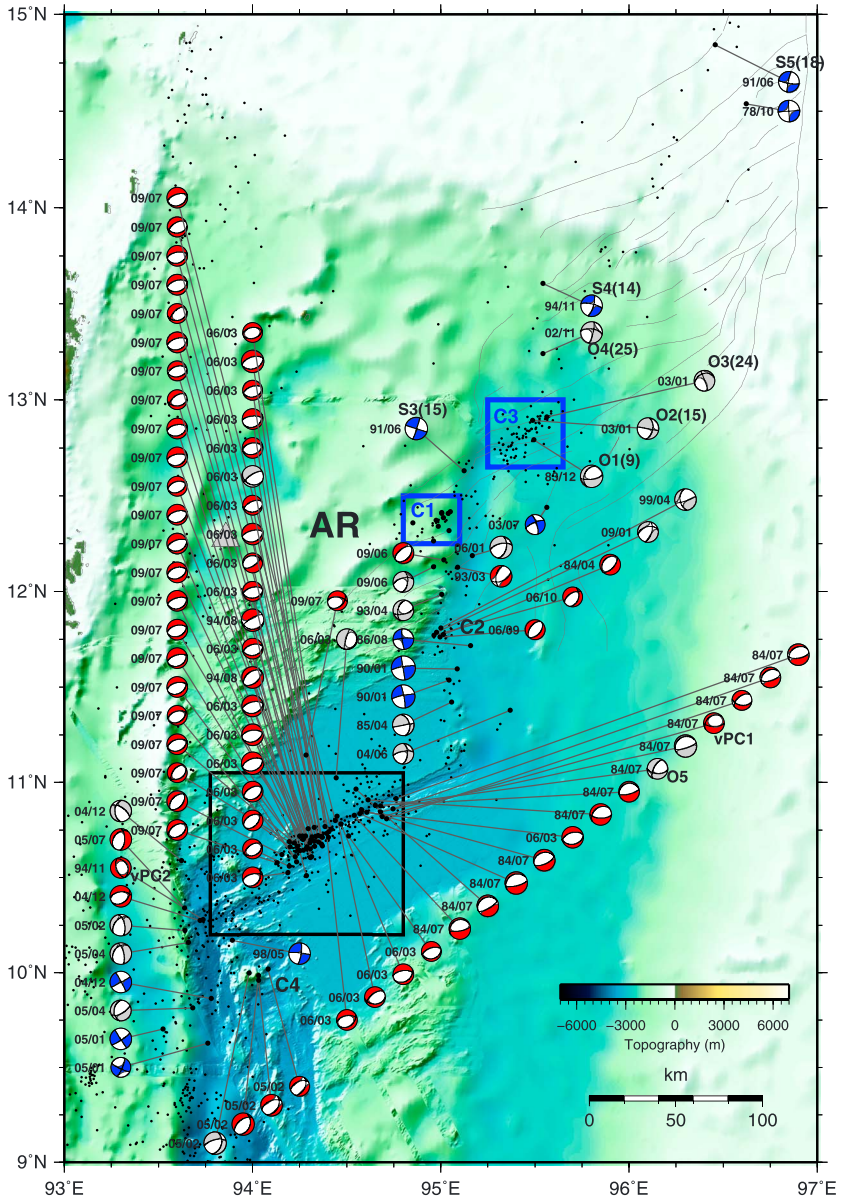

Figure 5. Map with DD locations (black dots) and associated global CMT solutions for the Andaman Back-Arc region. CMT solutions are color coded and annotated as in Figure 4. Solutions labeled O1–O4 and S3–S5 in the NE part are discussed in text, numbers in brackets next to the labels denote focal depths as reported in the EHB catalog. Solutions labeled vPC1-vPC2 indicate potential vertical-CLVD mechanisms. Background satellite bathymetry is sampled on a grid of 30 arc sec [*GEBCO_08 Grid*, http://www.gebco.net] with a horizontal resolution on the order of several kilometers in the Andaman Sea [*Smith and Sandwell*, 1997]. Bathymetry in the vicinity of the ABSC has a horizontal resolution of 200 m [*Kamesh Raju et al*., 2004]. Thin lines indicate the extensional horsetail system forming the southern termination of the Sagaing Fault as proposed by *Rangin et al*. [1999]. AR: Alcock Rise.

[14] Figure 4 demonstrates the improvement of the DD locations compared to the ISC/EDR bulletin locations for two clusters of earthquakes near 12.4°N/95°E (C1 in Figure 3) and 12.8°N/95.5°E (C3 in Figure 3). While the ISC/EDR epicenters widely scatter (Figure 4a), the DD locations resolve a NE-SW striking structure (Figure 4b), consistent with the fault strike of the CMT solutions and the NE-SW oriented structures present in the bathymetry data near the Alcock Rise (Figure 1). DD locations of cluster C3 (Figure 4d) show that the three sequences occupy distinct areas of the basin suggesting differences in their underlying tectonic mechanisms. Relative location errors, computed from 200 bootstrap samples drawn from the final residual vector for each event (see *Waldhauser and Ellsworth* [2000] for details), are on the order of few kilometers or less. They are shown in Figure 4 as horizontal projections of the 90% confidence ellipsoids. Relocations of events prior to the 1990s and back to 1964 are mainly or entirely based on bulletin pick data, and therefore the quality of the DD locations may also vary with time.

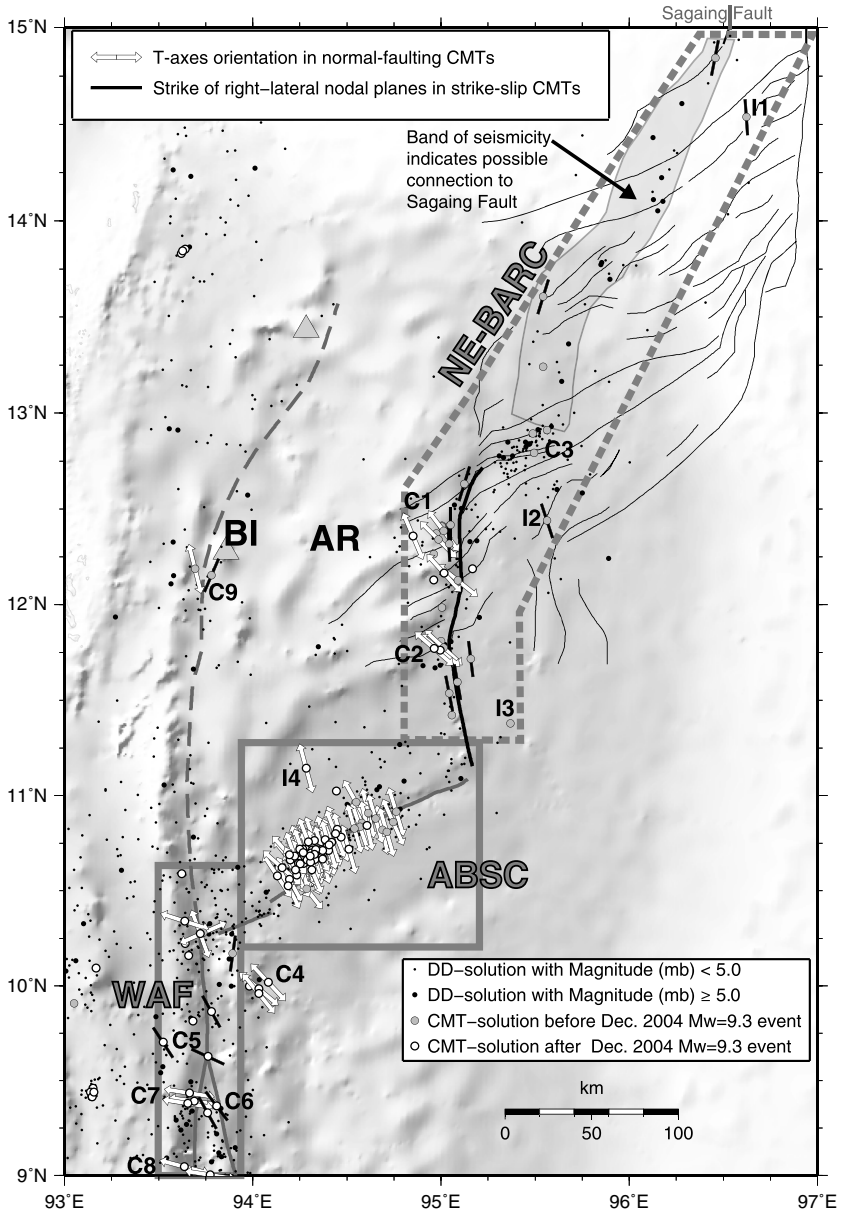

Figure 6. Plate boundaries and associated slip directions in the Andaman Sea based on DD relocations (black dots; focal depths ≤50 km), CMT solutions, and bathymetry data. Faults west of the spreading center are from *Curray* [2005]. Spreading segments are from *Kamesh Raju et al*. [2004]. Thin lines indicate the extensional horsetail system forming the southern termination of the Sagaing Fault as proposed by *Rangin et al*. [1999]. Direction of CMT *T* axes of normal-faulting events (where *P* axes plunge ≥60°) indicates direction of maximum extensional strain and is represented by white arrows. Black bars indicate strike of dextral nodal planes of the strike-slip events (where *B* axes plunge ≥60°). Areas outlined by gray lines define different sectors of the Andaman Sea as discussed in the text. AR: Alcock Rise; BI: Barren Island.

2.3. Assessment of Absolute Location Robustness

[15] Because the EHB locations are the reference base for the overall absolute location of the DD solutions, possible bias in the EHB locations would also affect the absolute position of the DD solutions. Such bias may result from deviations of the true structure from the 1-D velocity model ak135 used to locate the events (presence of slab, etc.) and bias in station geometry. Grid search results using the 3-D regional velocity model of *Widiyantoro and van der Hilst* [1997] indicate that our absolute locations are robust within 5 km. While relative depths are typically well constrained by differential depth and core phases, the absolute depths in our DD catalog are mostly constrained by depth phases from the EHB bulletin. More details on absolute location robustness are provided in section S.2 of the supporting information.

Table 1. Distribution of Seismic Moment Release M_0 From Global CMT Solutions in the Andaman Sea (Figure 4–6)[a]

Sector	Focal Mechanism	# CMTs	% of Total M_0
WAF	All	18	23
	SS	6	4
	NF	8	16
	OS	4	3
ABSC	All	62	34
	NF	58	31
	OS	4	3
NE-BARC	All	34	37
	SS	10	15
	NF	8	4
	OS	16	18

[a]The total seismic moment M_0 of all CMT solutions in the Andaman back-arc region (Figure 5) is $1.269 \cdot 10^{26}$ dyne cm. Groups of focal mechanisms are defined in the caption of Figure 4 (SS: strike slip, NF: normal fault, OS: oblique slip). Gray boxes in Figure 6 define sectors of seismicity (NE-BARC sector is outlined by dashed line). Clusters C4 and C9 outside of the three sectors (Figure 6) accommodate the remaining 6% of the total M_0.

3. Seismic Structure and Kinematics of the Andaman Sea Plate Boundary

[16] The relocated seismicity and CMT solutions (Figures 5 and 6) image a system of active normal and strike-slip faults that connect the right-lateral Sumatra, Seulimeum, and West Andaman transform faults in the southwest with the Sagaing Fault in the northeast, forming the present eastern edge of the Burma Plate [*Curray*, 2005; *Cochran*, 2010] (Figure 1). The majority of earthquakes occur along the extensional plate boundary in the ABSC (Table 1), with intraplate earthquakes (such as I1–I4 in Figure 6) accounting for less than 2% of the total seismic moment in the back-arc region. CMT solutions along the fault system connecting the ABSC with the Sagaing Fault in the northeastern back-arc (NE-BARC region in Figure 6) are sparser but bigger (i.e., lower b-value) relative to the ABSC (Figures S6 and S7, see section S.3 of the supporting information for more details on the b-value analysis), and earthquakes cluster in both space and time as demonstrated by clusters C1 and C2 (Figure 6 and Table 1). Earthquakes in clusters C1 and C2 locate east of the NS trending transform faults and seafloor depression and show primarily extensional failure along ~20 km long NE-SW striking faults. These faults abut the NS striking transform fault and presumed plate boundary (Figures 4b and 6).

[17] Cluster C1 is formed by a sequence of extensional events ($Mw = 4.8$–5.8) (N1–N8, Figure 4b) that started in July 2007 and lasted for less than a year. The distribution of magnitudes with time in Figure S3 suggests a foreshock-main shock-aftershock pattern, and the b-value of cluster C1 is close to 1 (Figure S7). The sequence was preceded, by 1 year, by two right-lateral, strike-slip earthquakes ($Mw = 5.1$ and 5.3) that ruptured the adjacent transform fault within 1 h of each other (S1–S2, Figure 4b). The structure and kinematics of the seismicity that forms cluster C2 are comparable to those of C1, suggesting a similar process ~60 km south of C1.

[18] Another distinct earthquake cluster is revealed in the northeastern part of the basin (C3, Figures 4d and 6). The position and orientation of this 35 km long cluster correlate with a NE-SW striking seafloor depression, which is interpreted as a short spreading axis by *Curray* [2005]. The majority of earthquakes associated with C3 occurred within three sequences (December 1983, orange; January 1984, yellow; January 2003, blue; Figure 4d) that occupy distinct areas. The 1983 sequence initiated in the center of the bathymetric depression and activated faults along the northern rim of the basin and beyond to the northeast. The 1984 and 2003 sequences flanked the 1984 sequence at its SW and NE terminations. The sequences in 1983 and 1984 have the character of earthquake swarms, whereas the first sequence in January 2003 indicates a main shock-aftershock pattern (Figure S4).

3.1. Spatiotemporal Characteristics of ABSC Seismicity

[19] Three major swarms that occurred in 1984, 2006, and 2009, and two smaller ones in 1973 and 1993 dominate the seismicity along the ABSC (Figures 2, S1, and S2 and Table 2). CMT solutions are almost exclusively pure normal-faulting mechanisms with some variation in strike and dip (Figures 5 and 6). The analysis of non-double-couple components of global CMT solutions, described in detail in section S.4 of the supporting information, identified a possible vertical compensated-linear-vector-dipole (CLVD) mechanism within the 1984 swarm (vPC1 in Figure 5). Figure 7a shows the high-resolution bathymetry data for the seismically active central part of the spreading ridge with DD locations superimposed (dots color coded according to swarm occurrence). Based on the bathymetry data and magnetic anomalies, the ABSC is divided into three segments: A, B, and C (brown lines in Figure 7a) [*Kamesh Raju et al.*, 2004].

Table 2. Statistics of Major Earthquake Swarms in the Andaman Back-Arc Spreading Center[a]

Start	On Spreading Segment	Duration of Total Activity (Days)	Duration of Main Activity (Days)[b]	# Events in ISC/ EDR + DD Location	# Events With CMT + DD Location	Sum of CMT Moments (10^{26} dyne cm)
1973/07/26[c] 04:23	A	1	1	6	0	-
1984/07/05 20:46	C	40	7	80	12	0.117
1993/08/23 18:53	A + B	10	2	21	0	-
2006/03/09 14:45	B + C	23	3	137	24	0.168
2009/07/26 06:45	B + C	3	3	52	24	0.104
					Sum:	0.424

[a]Spreading segments are defined in Figure 7.
[b]Duration of main activity is defined by consecutive days of ≥3 events per day.
[c]Dates are formatted as year/month/day.

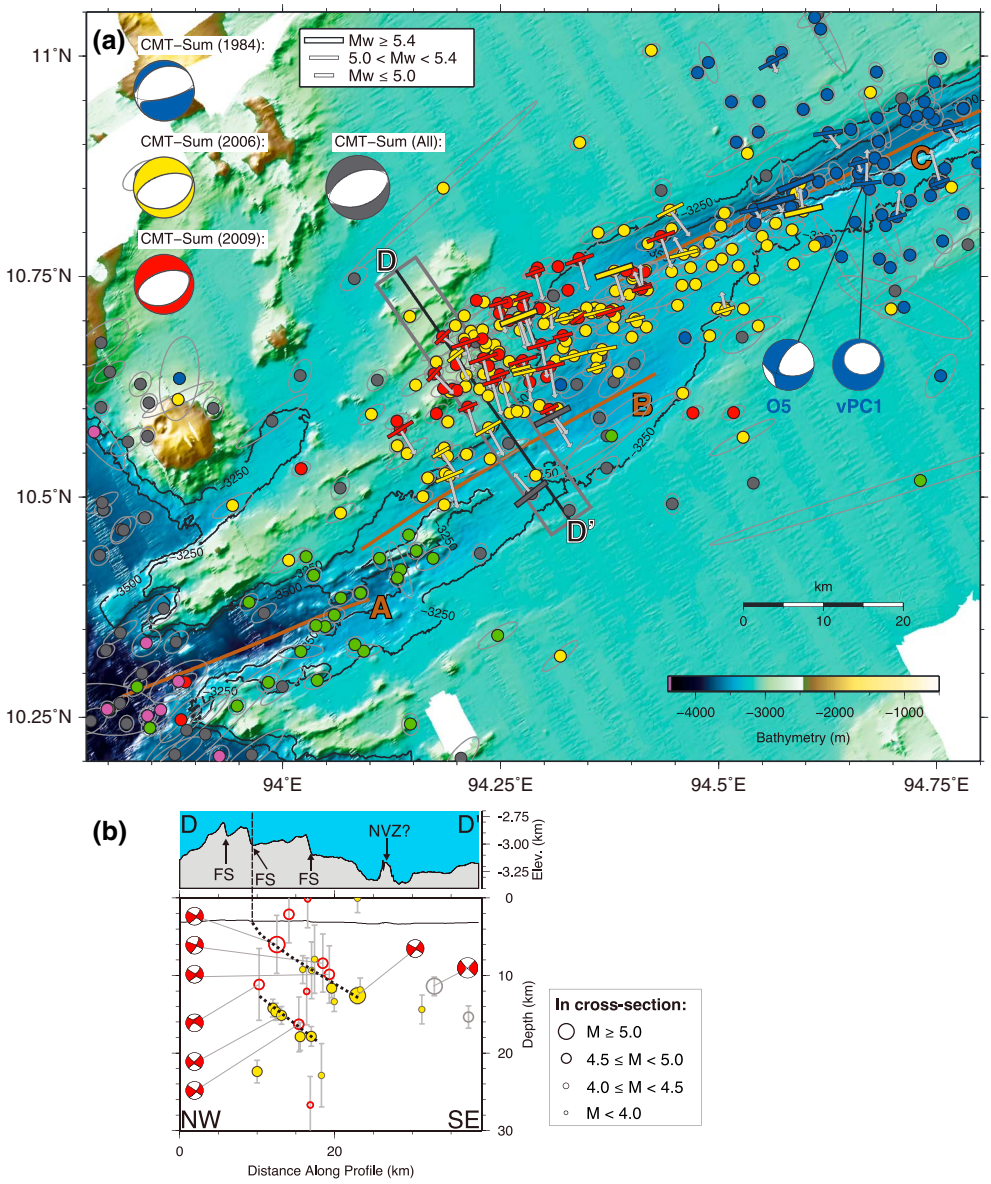

Figure 7. (a) Map with DD locations (dots) in the Andaman Back-Arc Spreading Center (see black box in Figure 5). Gray: background seismicity; magenta: seismicity in 1973; blue: seismicity in 1984; green: 1993; yellow: 2006; red: 2009. Gray ellipses indicate 90% confidence interval for relative locations derived from bootstrap analysis. Bars correspond to surface projections of *B* axes of global CMT solutions of normal-faulting events; gray arrows correspond to surface projections of the CMT slip vector (preferred fault plane); Beach-ball symbols indicate composite moment tensors of individual swarms and all CMT solutions. High-resolution bathymetry (grid of 100 m) is from *Kamesh Raju et al.* [2004]. Ridge segments A–C [*Kamesh Raju et al.*, 2004] are indicated by brown lines. D–D′ shows location of depth profile in Figure 7b for events included in box. (b) Depth cross-section along profile D–D′. Circles and dots are hypocenters using the same color scheme as in Figure 7a. Error bars indicate the 90% confidence interval of relative depth derived from bootstrap analysis. Global CMT solutions are shown as projections to the depth profile. Note vertical exaggeration of bathymetry cross-section. FS: Fault Scarp; NVZ: Neovolcanic Zone.

[20] The smallest swarm occurred in July 1973 (magenta dots in Figure 7a) at the western end of segment A. It contains six events, and its duration was less than a day.

[21] The swarm of July 1984 includes ~80 events (blue dots in Figure 7a) and occupied approximately 40 km of the central part of the eastern spreading segment C. This segment is characterized by a deep and narrow rift valley. Although thick sediment makes it difficult to recognize magnetic anomalies in the eastern part of ABSC, this segment is considered the oldest part of the ABSC [*Kamesh Raju et al.*, 2004]. The first recorded event (mb = 5.0) of the swarm occurred about 15 km north of the ridge axis and was immediately followed by two bigger events (mb = 5.4 and 5.3) located in the rift valley. About 48 h later, the main activity started in the rift valley and propagated from the center of segment C southwestward along the ridge (Figure 8). The

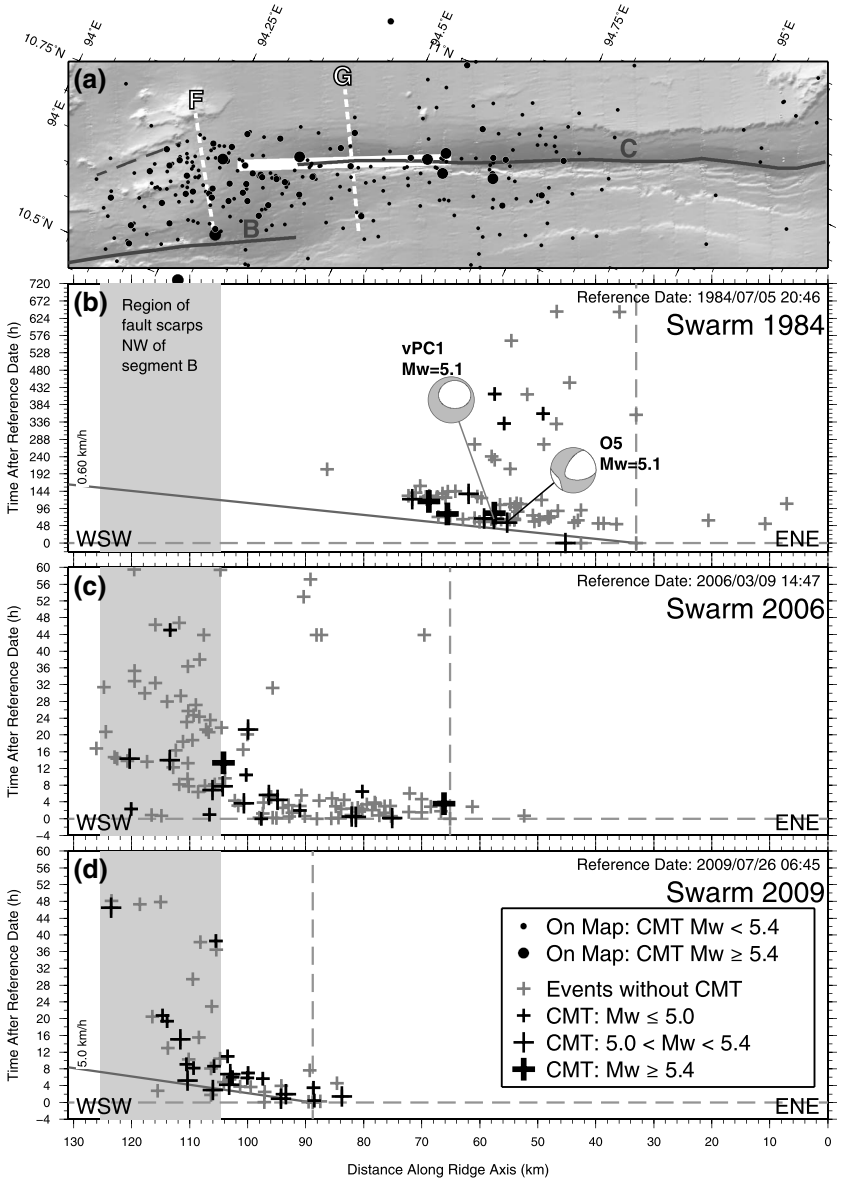

Figure 8. (a) Location of along-ridge profile and DD epicenters in the Andaman Spreading Center. Solid white line indicates along-strike extent of a hypothetical dike opening used for Coulomb-stress change modeling. Dashed white lines (F, G) indicate location of Coulomb-stress change profiles discussed in text. (b, c) Origin time versus distance along-ridge axis for three major swarms in the Andaman Spreading Center. Position of first event of each swarm is indicated by vertical dashed gray line. Black lines indicate possible propagation velocities. Focal mechanisms in Figure 8b indicate location and timing of oblique mechanism O5 and vertical-P CLVD mechanism vPC1 during the 1984 swarm.

activity persisted for more than a week, and a propagation velocity in the range of 0.2–0.6 km/h is derived. A composite solution of the moment tensors in this swarm results in a NE-SW striking normal fault with a marginal strike-slip component (Figure 7a) with the steeper of the two double-couple planes dipping SE. Two mechanisms (O5, vPC1 in Figures 5, 7a, and 8b) in the global CMT catalog deviate from the composite solution. Solution O5 has a small strike-slip component and vPC1 falls in the category of vertical-P CLVD mechanisms, which are mainly observed in volcanic regions and often interpreted as the result of dip-slip motion on volcanic ring-faults [e.g., *Shuler et al.*, 2013]. We obtain a b-value close to 2.0 (Figure S6) consistent with the result of *Mukhopadhyay and Dasgupta* [2008].

[22] A minor swarm occurred in August 1993 (green dots in Figure 7a) between segments A and B, east of the 1973 swarm. The main activity only lasted for a few days (Figure S2), and no CMT solutions are available for these events. The relocated epicenters spread over a distance of about 20 km, clearly disconnected from and to the west of the 1984 swarm.

[23] In March 2006, about 14 months after the December 2004 $Mw = 9.2$ event, the largest of the four swarms (Table 2), including ~130 events (yellow dots in Figure 7a) occurred at the western edge of segment C and north of segment B. The swarm filled the spatial gap between the 1984 and 1993 swarms. It

initiated approximately at the WSW end of the 1984 swarm on ridge segment C and propagated southwestward along the ridge, similar to the 1984 swarm but at much higher speed. Within 2 h, the swarm events covered a distance of about 50 km along the ridge (Figure 8). After about 8 h, seismic activity ceased in the rift valley of segment C. At the same time, intense activity started off-axis north of segment B and lasted for about 2 days before gradually decaying over the following 20 days. The seafloor morphology in that area shows SW-NE oriented lineaments and suggests fault scarps related to SE-dipping planes (Figure 7b). The composite moment tensor of this swarm corresponds to a NE-SW striking, pure normal fault with the shallower of the two double-couple planes dipping SE. The b-value of the 2006 swarm derived from mb reported in the ISC catalog is close to 2.0 (Figure S6).

[24] The 2009 swarm, while smaller (~50 events, Figure 7a), is similar to the 2006 swarm in many aspects. The affected area and spatiotemporal evolution of the activity is similar to the 2006 swarm, and the composite moment tensor is almost identical with the solution derived from the 2006 earthquakes. The strike of CMT *B* axes (indicated by thick lines in Figure 7a) for several events in the 2006 and 2009 swarm align remarkably well with the strike of the fault scarps seen in the bathymetry data north of segment B. Hypocenters plotted in a vertical cross-section normal to the strike of these fault scarps reveal at least two active faults that dip ~30° to the SE, consistent with the SE-dipping double-couple planes (Figure 7b). The intersection of the projection of the shallower of the two faults with the seafloor coincides with fault scarps seen in the bathymetry data. The b-value of the 2009 swarm derived from mb reported in the ISC catalog is close to 2.0 (Figure S6).

4. Discussion

4.1. Mode of Extension in the Andaman Sea

[25] While formation of trench-parallel back-arc basins is commonly associated with trench rollback, the oblique opening of the Andaman Sea (Figure 1) results from the combination of two extensional components. *Curray* [2005] decomposed the average spreading rates in the ABSC into a northward component (2.7 cm/yr) and a westward component (1.2 cm/yr). The dominant northward component compares well with slip rates observed along the Sumatra fault [*Curray*, 2005], and its driving force seems to be the northward dragging of the Burma sliver plate by the trench-parallel component of convergence. Slip rates along the northern portion of the Sumatra fault are on the order of 2.7–2.5 cm/yr [*Sieh and Natawidjaja*, 2000; *Genrich et al*., 2000]. Present-day geodetic slip rates along the Sagaing Fault in Myanmar are on the order of 1.8 cm/yr [*Vigny et al*., 2003; *Maurin et al*., 2010] and therefore smaller than the average long-term northward component of the spreading rate. This difference in slip rate can be explained by the partitioning of motion between the India-Burma and Burma-Sunda plates, and the slip rates predicted by such a model agree to a first order with the observed rates [*Gahalaut and Gahalaut*, 2007]. Northward motion might also be partially absorbed by diffuse fault systems such as the extensional horsetail structure proposed by *Rangin et al*. [1999] (Figures 1, 5, and 6). The smaller westward component of the spreading rate (1.2 cm/yr) likely results from rollback, modulated by recurrent stresses due to coseismic slip and afterslip on the plate interface.

[26] The West Andaman fault (WAF) system southeast of the ABSC seems to accommodate both dextral and westward extensional motion (Figure 6), and the partitioning appears to be correlated in time with coseismic slip and afterslip of the $Mw = 9.2$ Sumatra-Andaman earthquake of December 2004. Extensional mechanisms along the WAF system between 9.0°N and 10.5°N occur almost exclusively in the months after the 2004 earthquake (Figure 6) and correlate in space with a peak in coseismic and postseismic deformation and moment release [*Chlieh et al*., 2007]. This change from dextral toward extensional regime of the WAF system was already noticed by others [e.g., *Engdahl et al*., 2007; *Cattin et al*., 2009]; however, whether or not extensional and strike-slip motion is partitioned on the same fault (e.g., the WAF) cannot be answered conclusively. Based on bathymetry and reflection seismic profiles [*Curray*, 2005; *Kamesh Raju et al*., 2007; *Cochran*, 2010], the WAF is expected to dip steeply toward the east. In fact, fault planes associated with dextral slip (such as C5 and C6 in Figure 6) show dip angles of 80° to 90°. Fault planes associated with eastward dipping normal faults (such as C7 and C8 in Figure 6), however, have shallower dip angles of 50° to 60°. The difference in fault dip suggests that the extensional strain might be accommodated on splay structures of the master strike-slip fault.

[27] The inferred plate boundary connecting the ABSC with the Sagaing Fault consists of a right-lateral transform with prominent extensional bends (solid black line within dashed region in Figure 6). The contribution to overall back-arc extension, as indicated by the distribution of extensional CMT solutions and seismic moment (Table 1 and Figure 6), seems minor. A large fraction of the seismic moment release in this region is accommodated by oblique-slip mechanisms (Table 1) suggesting the presence of young structures, where strain partitioning is not yet developed. Normal-fault earthquakes, as observed in clusters C1 and C2 (Figures 4b and 6), accommodate additional extension at the eastern edge of the Alcock Rise on NE-SW striking faults [see also *Rangin et al*., 1999; *Curray*, 2005]. These faults consistently locate west of the inferred plate boundary that hosts the strike-slip events (Figures 4b and 6). The spatiotemporal evolution of these earthquakes and the fact that the normal-faulting events closest to the transform fault have a significant strike-slip component (Figure 4b) suggest that the extensional events accommodate additional bending-related residual stresses from slip on the east veering transform plate boundary in that region. The NW-SE orientation of *T* axes of the extensional earthquakes N2–N8 in Figure 4b agrees with the *T* axes orientation observed for the two nearby strike-slip events S1–S2 and is similar to the general trend of the ABSC (Figure 6).

[28] Seafloor morphology and the orientation of relocated seismicity in combination with the strike of right-lateral fault planes such as S1–S3 suggest that the inferred transform fault (solid black line within dashed region in Figure 6) links the ABSC with the short spreading segment of cluster C3 (Figures 4b, 5, and 6). Earthquake swarms in 1983 and 1984 in cluster C3 are indicative of active spreading processes involved in the formation of this basin. Three available moment tensor solutions (O1–O3, Figure 4d), however, indicate oblique slip. Oblique slip likely contributes to the basin development similar to transtensional mechanisms proposed for basin formation in the Marmara Sea [*Seeber et al*., 2006].

[29] Seismicity is more diffuse between the short spreading segment of cluster C3 and the Sagaing Fault (Figures 5 and 6), and no clear connection between both structures is resolved. *Chamot-Rooke et al*. [2001] proposed an eastward connection of the short spreading segment of cluster C3 to a series of grabens, forming the horsetail termination of the Sagaing Fault system (Figures 5 and 6). The strike of right-lateral fault planes such as of O2–O4 and S4 (Figure 5), however, deviates significantly from the general WSW-ENE strike of the proposed horsetail system. Well-constrained hypocenters in the EHB catalog report focal depths in the range of 14–25 km for these events (Figure 5), which places them in the lower part of the crust. Relocated seismicity is concentrated along a band in the western end of the horsetail system (Figure 6). Therefore, we cannot rule out a possible connection to the Sagaing Fault by a system of faults in the underlying basement (outlined by gray shaded area in Figure 6).

[30] The distribution of extensional CMT solutions and seismic moment in the Andaman Sea suggests that back-arc extension occurs primarily in the ABSC (Table 1 and Figure 6). To quantify the direction and the amount of extension accommodated by seismic slip on normal faults in the ABSC, we calculated the short-term spreading rate by following the calculations of *Guzmán-Speziale and Ni* [1993] with modified model assumptions and updated global CMT solutions. The direction of maximum extensive strain is defined by the eigenvector $\boldsymbol{e_1}$ associated with the largest eigenvalue λ_1 of the summed moment tensor $\underline{\boldsymbol{M_s}}$ of all normal-faulting events at the ridge. The spreading rate v can be derived from the following:

$$v = \frac{1}{2\mu\tau L h}\lambda_1, \tag{1}$$

with τ being the time interval, μ the shear modulus ($3 \cdot 10^{10}$ N/m^2), L the length of the ridge, h the maximum depth of the seismogenic layer, and λ_1 the largest eigenvalue of $\underline{\boldsymbol{M_s}}$. We assume that recent and current extension correlates with normal-fault earthquakes along segments C and B of the ABSC, and L is about 84 km (Figure 7a). The cross-section in Figure 7b suggests a seismogenic layer of about 18 km; however, these events are off-axis and represent reactivation of existing faults. Instead, we use a seismogenic layer h of 10 km, a value commonly assumed to be the maximum focal depth at mid-ocean rifts [*Huang and Solomon*, 1988]. Because the actual depth of the seismogenic layer lies somewhere between 10 and 18 km, the spreading rate derived from equation (1) with $h = 10$ km should only be considered as an upper bound rather than a best estimate. We sum up all CMT solutions with P axes plunging ≥60° (normal-faulting type). We find 57 of these events between 1984 and 2009 ($\tau = 26$ years). The largest eigenvalue λ_1 of $\underline{\boldsymbol{M_s}}$ is $3.301 \cdot 10^{18}$ Nm. The direction of maximum extensive strain defined by eigenvector $\boldsymbol{e_1}$ is N22°W, which is close to the value of N19°W found by *Guzmán-Speziale and Ni* [1993]. It also compares well to the long-term spreading direction of N25°W derived by *Curray* [2005] from reconstruction of the ABSC over the past 4 Myr. Using equation (1), the maximum bound on the tectonic contribution to the spreading rate v of our model is about 0.25 cm/yr, which is about 5 times higher than what *Guzmán-Speziale and Ni* [1993] obtained (0.05 cm/yr), but more than one order of magnitude smaller than the long-term opening rate of 3.0–3.8 cm/yr [*Kamesh Raju et al*., 2004; *Curray* 2005]. Since the 1984 and 2009 swarms bracket the observation period, τ might also be underestimated. Thus, seismic slip on normal faults accounts at most for 7–8% of the long-term opening rate. Similar to *Guzmán-Speziale and Ni* [1993] and *Solomon et al*. [1988], we interpret the deficit in seismically accommodated extension as indication for aseismic processes. The deficit in seismic moment and the morphology of the ABSC supports an active spreading system, where extension (driven by far field forces) is largely accommodated by intrusion of new crust along the central neovolcanic zone. The proposed formation of new crust is further supported by magnetic anomalies from shipboard surveys [*Kamesh Raju et al*., 2004] and satellite data (Figure S9). Recent industry seismic reflection data image many sills below the basement, also indicative for ongoing diking and intrusion processes [*Singh et al*., 2010]. The thick sedimentary cover of the northeastern ridge segment likely acts as a blanket for volcanic eruptions and hydrothermal circulation, suggesting an accretionary process different from typical oceanic spreading [*Singh et al*., 2010].

4.2. Structure and Fault Geometry of the ABSC

[31] Similar to slow-spreading ridges in the Mid-Atlantic, the morphology of the ABSC is characterized by a distinct rift valley bounded by a series of scarps and steplike terraces, which are apparent in the high-resolution bathymetry maps on either side of the rift (Figures 7a and 8) and in cross-axis bathymetry profiles (Figure 9). We interpret these fault scarps as expressions of inward facing normal faults. These faults are indicative of tectonic extension processes (including faulting, uplifting, and tilting of blocks) and may contribute significantly to the formation of the axial depression of slow-spreading ridges [e.g., *Mutter and Karson*, 1992]. Fault scarps in the inside corners of segments B and C appear to have larger throws than elsewhere along the ABSC (Figure 9).

[32] The role of inward facing normal faults in the architecture of the rift valley is confirmed by two single-channel seismic reflection profiles, penetrating the first few kilometers of the crust [*Kamesh Raju et al*., 2004, Figure 10]. A profile across segment C (close to profile 20 of Figures 9 and 10a), suggests a full graben structure. It images inward facing normal faults with corresponding fault scarps in the bathymetric cross-section of profiles 20 and 21 (Figure 9). A second seismic profile close to DD′ of Figure 7b across segment B indicates inward facing normal faults southeast of the rift valley. To the northwest, *Kamesh Raju et al*. [2004] interpret near seafloor reflections as shallow basement; however, faults are not resolved in this part of the seismic image.

[33] Seismicity along profile DD′ suggests moderately dipping faults north of segment B (Figure 7b). In contrast, seismicity profiles across segment C provide no constraint on fault dip. Insufficient depth resolution of hypocenters due to fewer and lower quality data in 1984 may be a factor, in addition to possible along-strike discontinuities between faults. Information on fault dips across segment C is derived from CMT double-couple solutions. The preferred fault planes are inward facing, following observations from the two seismic profiles and the seismicity profile DD′. We

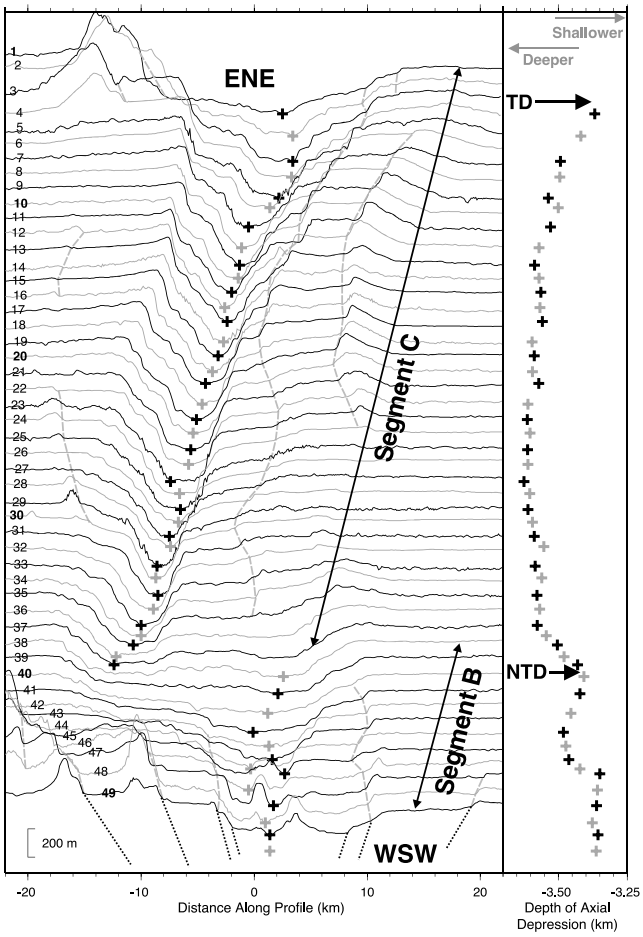

Figure 9. (left) Bathymetry profiles across the ABSC derived from the high-resolution grid of *Kamesh Raju et al*. [2004]. Tracks and origins of selected profiles are shown in Figure 10a. Numbers on the left indicate index of profile. Spacing between profiles is 2.5 km. Crosses mark position of maximum axial depression on each profile. Gray dashed lines indicate possible fault scarps; black dotted lines suggest notional geometry of normal faults. (right) Depth of maximum axial depression of each profile. Black arrows indicate position of ridge discontinuities (TD: Transform Discontinuity; NTD: Nontransform Discontinuity).

choose southward dipping fault planes for earthquakes that locate northwest of the ridge axis and northward dipping planes for earthquakes located southwest of the axis. We do not consider events located in the offset area between segments B and C, due to the lack of information on fault dip direction in this area. Our preferred fault planes are shown as gray arrows in Figure 7a, representing projections of slip vectors calculated from strike, dip, and rake of the preferred double-couple solution. Steeply dipping faults (50°–75°) occur preferentially in the central part of segment C, where they are likely associated with the main boundary faults of the inner floor of the rift valley. Similar mechanisms were proposed for the largest earthquakes on the Mid-Atlantic Ridge [e.g., *Bergman and Solomon*, 1990]. The moderately dipping fault planes (27°–45°) north of segment B (Figure 10b) are consistent with the dip of the proposed off-axis faults observed along profile DD′ in Figure 7b.

[34] The offset between segments C and B is small, ~13 km, and appears to be a nontransform discontinuity (Figures 7a and 9). It subdivides the deep, distinct, narrow valley in segment C from the shallow, rugged depression in segment B (Figure 9). Similar nontransform discontinuities are found in parts of the Mid-Atlantic Ridge [e.g., *Sempere et al*., 1990], where they are associated with lateral differences in the magma supply [e.g., *Macdonald et al*., 1991]. Alternative models propose mechanical deformation to explain segmentation at slow-spreading ridges [e.g., *Mutter and Karson*, 1992]. Prominent expressions of mechanical deformation are oceanic detachments at inside corners of jogs along slow-spreading ridges [e.g., *Tucholke and Lin*, 1994; *Escartin et al*., 2008]. The spatial correlation between large-offset faults and ridge discontinuities in the ABSC (Figure 9) suggests the involvement of mechanical processes, even though fault scarps north of segment B are quite different from typical oceanic detachments. Whether or not the offset between C and B is of "magmatic" or "mechanical" origin remains unclear. On a broader scale, ridge segmentation is typical of oblique spreading systems dominated by remote tectonic stresses [e.g., *Abelson and Agnon*, 1997] and might indicate a re-adjustment of the ridge as discussed later.

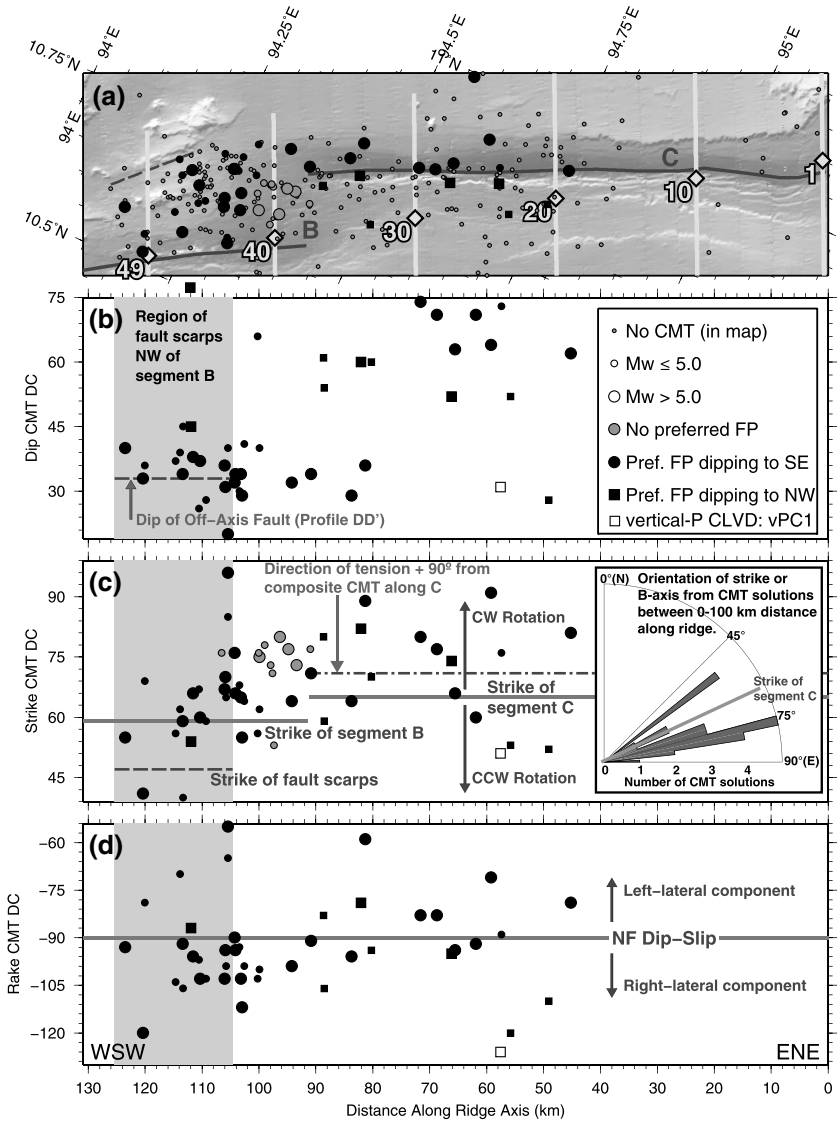

Figure 10. (a) Location of along-ridge profile, DD epicenters, preferred fault planes, and tracks of bathymetry profiles shown in Figure 9. (b–d) Dip, strike, and rake of preferred fault planes along the ridge axis. CMT solutions for which a preferred fault plane has been determined are indicated by black bold dots and squares (dots: preferred fault plane dipping to SE; squares: preferred fault plane dipping to NW). White square indicates vertical-P CLVD mechanisms vPC1. For CMT solutions without preferred plane (gray dots), azimuths of *B* axes are shown in Figure 10c. Dash-dotted line in Figure 10c indicates direction of maximum extensional strain plus 90° as derived from composite CMT solutions along segment C. Rose diagram in Figure 10c shows orientation of fault strike or *B* axis of CMT solutions along segment C.

[35] The ABSC displays many of the key features of mid-ocean ridges, yet some differences are noteworthy. In contrast to mid-ocean ridges, the transform and nontransform discontinuities at the ends of segment C coincide with minimum axial depths. Also, segment C does not exhibit the typical axial high (Figure 9), but thick sediment masks basement morphology along this segment. The ABSC is unusual among spreading ridges in being surrounded by sediment sources and thus receiving not only high but also spatially variable sedimentation. Changes in sediment cover accounts for some of the differences in sea floor morphology along the ABSC [*Kamesh Raju et al*., 2004; *Curray*, 2005; *Singh et al*., 2010] but may also account for structural differences. In models proposed for rifting in the Gulf of California, deposition of sediments promotes narrow rifting [*Lizarralde et al*., 2007; *Bialas and Buck*, 2009]. Accordingly, the thick sediment cover deposited by turbidity currents that are reaching segment C, but not B, may have led to the observed along-axis difference in the extensional styles between these segments.

4.3. Kinematics of the ABSC

[36] Although some earthquakes in the 1984 sequence are off-axis, the main activity within this swarm concentrates beneath the rift valley on steeply dipping faults (Figures 7a and 10b). The seismic activity propagates over 40 km along the rift from ENE to WSW (Figure 8b) with a velocity of about 0.6 km/h, comparable to propagation velocities observed in

other rift systems (Iceland: 1.8 km/h [e.g., *Einarsson and Brandsdottir*, 1980]; Afar: 1.1 km/h [e.g., *Ayele et al*., 2009]). Swarms associated with seafloor spreading events along the Juan de Fuca and Gorda ridge in the Eastern Pacific show very similar migration rates of 0.2 to 2.0 km/h [*Dziak et al*., 2007]. Magmatic processes are predicted by the deficit in seismic moment, high b-values, the presence of seafloor spreading magnetic anomalies [*Kamesh Raju et al*., 2004], and seismic reflection data of *Singh et al*. [2010]. Therefore, we interpret the 1984 swarm as expression of a dike intrusion propagating laterally toward WSW. The occurrence of exclusively normal-faulting events on the main boundary faults of the inner rift floor is consistent with volcanic-spreading events on mid-ocean ridges [e.g., *Tolstoy et al*., 2001] and can be accounted for by the tensile stress field that forms above the propagating dike [*Rubin*, 1992]. The location of the vertical-P CLVD mechanisms vPC1 in the 1984 swarm coincides with the oblique mechanism O5 (Figure 7a). Event O5 occurred on 8 July (05:26) followed by event vPC1 about 11 h later (Figure 8b). As proposed by *Ekström* [1994], such vertical-CLVD mechanism can be explained by dip-slip motion on volcanic ring-faults. *Shuler et al*. [2013] found a strong correlation between the occurrence of vertical-CLVD mechanisms and volcanic unrest, where vertical-P mechanisms generally occur after eruptions. The location and timing of event O5 and vPC1 might therefore be indicative for volcanic processes such as deflating or collapse of a magma chamber in the center of segment C during the swarm.

[37] In contrast to the 1984 sequence, earthquakes within the 2006 swarm occurred nearly concurrently (within 2 h) over more than 50 km across the western part of segment C beneath the rift valley, followed by an increased seismic activity in the fault scarp region north of segment B (Figure 8). If there were a propagation, it would have velocities >20 km/h, much higher than known lateral dike propagation velocities. The instantaneous occurrence of earthquakes is better explained as the consequence of near-simultaneous injections vertically from an axial magma lens, as proposed by *Dziak et al*. [2009]. Studies by *Cattin et al*. [2009] and *Sevilgen et al*. [2012] suggest that a critical stress regime may have built up in the back-arc due to the December 2004 $Mw = 9.2$ earthquake. Stress calculations show that the megathrust rupture increased the Coulomb stress on normal faults within the ABSC region. The Coulomb-stress increase in the ABSC derived by *Cattin et al*. [2009] and *Sevilgen et al*. [2012], however, is very small (about 0.2–0.3 bar) and does not explain the lag of 14 months between the 2004 rupture and the 2006 swarm.

[38] In order to compare the amplitudes of the post-2004 regional stress change to local stresses resulting from a dike intrusion, we modeled the Coulomb-stress change due to a hypothetical tensile dike opening at the location of the 2006 earthquake swarm using the COULOMB software package [*Stein*, 1999]. The modeled dike assumes a typical opening of 1 m and a height of 1.5 km [e.g., *Buck et al*., 2006; *Dziak et al*., 2009]. The along-strike extent of the modeled dike beneath segment C is derived from the distribution of hypocenters within the first 4 h of the 2006 swarm, and it is shown as a solid white line in Figure 8a. Its vertical position is based on seismic reflection profiles [*Singh et al*., 2010] and ranges from 4.0 km to 5.5 km depth (from seabed). The average positive Coulomb-stress change on axial normal faults (receiver fault: strike = 73°, dip = 58°, rake = −92°) above (and below) the opening dike at profile G in Figure 8a (depth range 0–20 km) is 3.6 bar. This value significantly exceeds possible coseismic stress perturbations that may have originated from the December 2004 rupture in the ABSC. Dike opening also leads to positive Coulomb-stress changes on the proposed moderately dipping normal faults (receiver fault: strike = 63°, dip = 36°, rake = −96°) in the off-axis region. The average positive Coulomb-stress change at the location of profile F in Figure 8a (depth range 0–20 km) is 0.4 bar, comparable to coseismic stress perturbations predicted by *Cattin et al*. [2009] and *Sevilgen et al*. [2012] for the December 2004 $Mw = 9.2$ earthquake. As shown in section S.6 of the supporting information, the overall results are rather independent of the details of the chosen dike geometry.

[39] Based on the above, we argue that the primary driver for the 2006 swarm was a magmatic intrusion, probably vertically injected from an axial magma lens beneath the WSW part of segment C. Earthquakes on moderately dipping off-axis faults may have been triggered by stress changes from the magmatic intrusion as well as from the primary sequences of earthquakes on axial faults in the rift valley along segment C. Similarities in location, b-values and the spatiotemporal behavior of seismicity suggest a similar mechanism for the 2009 swarm, although the propagation velocity in the 2009 swarm (on the order of a few kilometers per hour) appears lower than in the 2006 sequence and somewhat closer to values typically associated with lateral dike intrusion. Aseismic opening of the Andaman Sea at a rate of 3.8 cm/yr would require dike injections about every 25 years (assuming a typical dike thickness of ~1 m), which is roughly consistent with the period between the 1984 and the 2006/2009 swarms. No additional swarm was identified in the ISC catalog between 1964 and 1984 along segment C. Differences in the apparent migration rates of the three swarms, however, seem to hint that properties of injections such as dike width might not be uniform and that there is not a simple horizontal propagation but a combination of horizontal propagation and vertical injections. The westward propagation of dike intrusions and the potentially vertical injection during the 2006 event also implies the existence of several magma lenses beneath segment C, rather than one magma supply in the center of the segment. The WSW propagation of the swarms as well as the seismic activity within each swarm, on the other hand, suggest an "unzipping" of segment C from ENE to WSW, consistent with the proposed long-term westward propagation of the spreading center [*Kamesh Raju et al*., 2004]. Whether or not the 2006/2009 intrusion events have been triggered by the 2004 $Mw = 9.2$ Sumatra-Andaman earthquake remains unclear. Volumetric expansion in the back-arc region due to the megathrust earthquake as proposed by *Walter and Amelung* [2007] in combination with fluid-diffusion processes might be mechanisms to explain the delay of 14 months.

4.4. Strain Partitioning in a Non-orthogonal Ridge-Transform System

[40] The net long-term spreading direction in the ABSC is about N25°W [*Curray*, 2005] and therefore nearly normal to the general trend of the ridge but oblique to the adjacent

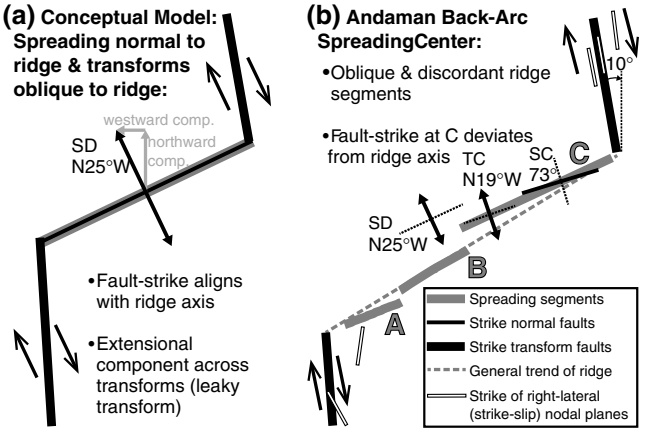

Figure 11. (a) Conceptual end-member model of non-orthogonal ridge-transform geometry. SD: long-term spreading direction [*Curray*, 2005]. Trend of ridge and transform faults are based on the ABSC geometry. (b) Summary of the ridge geometry of the ABSC. TC: direction of composite tension axis of CMT solutions at segment C; SC: median strike of nodal planes at segment C (inset Figure 10c).

transforms, as illustrated by the conceptual end-member model displayed in Figure 11a. To study how and to which degree strain is partitioned within such a non-orthogonal system, we begin with a detailed analysis of nodal planes and slip vectors from global CMT solutions in the ABSC. In Figures 10c and 10d, we plot strike and rake of the preferred (inward dipping) double-couple nodal planes with respect to their position along the ridge. For solutions without preferred planes (events in the overlapping zone between segments C and B), we plot the directions of *B* axes instead of fault strike (gray dots in Figure 10c).

[41] Nodal planes along segment C suggest clockwise misalignment with respect to the ridge axis (shown as solid line in Figure 10c), with deviations up to 25°. The median strike of preferred planes and directions of *B* axes along segment C is 73°, which corresponds to a deviation of 8° from ridge parallel as shown by the rose diagram in Figure 10c. The direction of the principal tensile strain derived from the composite moment tensor of CMT solutions along segment C (shown as dash-dotted line in Figure 10c) indicates a similar clockwise deviation of about 6° from ridge normal.

[42] To the WSW, fault strike of earthquakes in the fault scarp region and along segment B appear to align with the strike of segment B (median strike of preferred planes between 106 and 130 km in Figure 10c is 60°), and the inferred tension direction is close to normal to the ridge axis (Figures 6, 7a, and 10c). Two solutions, however, are anticlockwise misaligned. No CMT solutions are available for earthquakes located at spreading segment A.

[43] The rakes of preferred nodal planes distribute around −90° (Figure 10d) indicating pure dip-slip normal faulting. A systematic shift toward minor dextral components of slip vectors is apparent in the fault scarp region (rake about −105°). Few individual solutions along the ridge indicate larger deviation from pure dip-slip mechanisms (rake of about −120° and −60°, respectively).

[44] The conceptual model of Figure 11a agrees well with the general characteristics of the ABSC. However, while the spreading direction (SD in Figure 11) is perfectly normal to the strike of segment C, it is slightly oblique to segments A, B, and the general trend of the ridge axis (Figure 11b). The angle between the spreading direction and the normal to the general trend of the ridge axis is only about 6°, much smaller than values typically considered as oblique spreading [e.g., *Abelson and Agnon*, 1997]. Thus, we conclude that dip-slip normal faulting and the N22°W direction of maximum extensive strain of the cumulative CMT solution along the ridge are consistent with ridge-normal spreading. The N-S oriented troughs on either end of the ABSC (Figures 5 and 6) might be expressions of the "leaky" character of the adjacent transforms, due to westward extension across the strike-slip faults [e.g., *Menard and Atwater*, 1968; *Thompson and Melson*, 1972; *Taylor et al*., 1994].

[45] As illustrated in Figure 11b, the ridge is fragmented into three discordant segments obliquely oriented to its general trend. Such (second order) ridge segmentation is predicted by the crack model of *Abelson and Agnon* [1997] for oblique spreading systems dominated by remote tectonic stresses. The possible clockwise deviation of fault strike (SC) from the maximum extensive strain (TC) and the spreading direction (SD) along segment C (Figures 10c and 11b) suggest that the horizontal principal compressive stress axes ($S_H > S_h$) are oblique to both the spreading direction and the trend of the ridge, consistent with the "transtensional" model of *Tuckwell et al*. [1996]. In their model, extensional fractures and normal faults form normal to the minimum principal compressive stress S_h but oblique to ridge and plate vector. The extensional faults and dikes may form en-echelon arrays along the ridge axis. Thus, the observed misalignment of our nodal planes might indicate a similar en-echelon arrangement of dikes along segment C. But the observed 8° deviation of the median fault strike from ridge parallel along segment C might not be resolvable. Differences of 5–7° between moment tensors can be introduced by approximations in the modeling [e.g., *Hjörleifsdóttir and Ekström*, 2010], and studies comparing source parameters of different catalogs report uncertainties of 5–7° in moment tensors for the best CMT solutions [*Kagan*, 2003]. Based on a similar study, *Helffrich* [1997] concluded that the slip-vector uncertainty of a typical shallow earthquake is 14°. It is unlikely, however, that uncertainties in the moment tensor or slip vector are solely assigned to the fault strike component. The rather good agreement between fault strike and ridge orientation along segment B suggests that the observed misalignment along C is consistent with the overall discordant orientation of ridge segments B and C.

[46] Whether or not such non-orthogonal ridge-transform systems represent stable configurations over time or adjust toward orthogonal geometries remains controversial [e.g., *Lachenbruch and Thompson*, 1972; *Lachenbruch*, 1976; *Atwater and Macdonald*, 1977; *Tanaka and Fujii*, 1991]. In the Andaman Sea, structures are in place to lock geometry and direction of spreading. For instance, the position and geometry of transforms in the ABSC-system seem to be controlled by plateaus like the Alcock Rise, where the plate boundary follows the shape of its eastern edge (Figure 6). The initial NE-SW orientation of the spreading ridge is probably reflecting preexisting structures within these plateaus, similar to normal faults imaged by clusters C1 and C2. The

clockwise deviation of ridge segments A and C from the general trend of the ridge as well as possible clockwise deviation of fault strike and maximum extensive strain along segment C suggest that the segment geometry is not in equilibrium with current plate-motion demands and thus indicate ongoing readjustment of the ridge. Reorientation might occur by rift propagation [e.g., *Hey et al*., 1988], for instance, along segment C, which seems to be the most appropriately oriented ridge segment for the current spreading demands. Such a rift propagation concept would be consistent with the concentration of earthquakes beyond the SW end of segment C and the WSW migration of swarms.

5. Conclusions

[47] Teleseismic cross-correlation based double-difference relocation of seismicity in the Andaman Sea reveals insight into the spatial and temporal structure and dynamics of this extensional plate-boundary system. The new data image NE-SW trending active normal faults at the eastern edge of the Alcock Rise, which accommodate the NW-SE directed extension in the Andaman Sea. These normal faults are located west of the master plate boundary, which is inferred from N-S trending transform faults connecting the Andaman Back-Arc Spreading Center (ABSC) with the Sagaing Fault. Seismicity and seismic moment release suggest that back-arc extension is primarily accommodated within the ABSC. However, the short-term spreading rate derived from extensional moment tensors account for less than 10% of the long-term 3.0–3.8 cm/yr spreading rate. The deficit in seismic strain supports the concept of a spreading system, where extension is largely accommodated by formation of new crust.

[48] Episodes of dike intrusions are proposed as the primary driver for three major earthquake swarms in the ABSC. Directivity and migration velocities of seismicity in the 1984 swarm are interpreted as expression of a tensile stress field that forms above a lateral dike intrusion initiated in the central part of segment C, propagating toward WSW. High b-values of about 2 and the occurrence of a potential vertical-CLVD mechanism in the center of segment C are additional hints for a magmatic origin of the 1984 swarm. Swarms in 2006 and 2009 initiated at the WSW end of segment C and show similar propagation toward WSW. Coulomb-stress modeling suggests that dike opening and axial earthquakes triggered seismic activity on moderately inward dipping off-axis faults north of segment B. The period of about 25 years between the 1984 and 2006/2009 swarms is consistent with the long-term spreading rate of 3.8 cm/yr (assuming a dike thickness of 1 m and purely aseismic opening).

[49] The spreading direction in the ABSC over the past 4 Myr appears to be close to ridge normal but oblique to the adjacent transforms. The non-orthogonal ridge-transform geometry results in the formation of "leaky transforms," consistent with NS oriented deep troughs evident in the bathymetry on either side of the ABSC. In particular, the West Andaman fault system accommodates westward extension in the month after the $Mw = 9.2$ Sumatra-Andaman earthquake of December 2004. A possible systematic skew in slip vectors suggests an en-echelon arrangement of extensional structures in the eastern part of the ABSC, which indicates that segment geometry is not in equilibrium with current plate-motion demands and thus ongoing readjustment of the ridge.

[50] **Acknowledgments.** We thank Roger Buck, Göran Ekström, and Jochen Wössner for helpful discussions. Comments by the associate editor, Frederik Tilmann, and two anonymous reviewers helped to improve the manuscript. This work was supported in part by the National Science Foundation under grants EAR-06-08739 (T.D., F.W., E.R.E.) and OCE-0927024 (T.D., J.C., F.W., K.K.-R.). The LDEO contribution number is 7689. Seismic waveform data were obtained from the Incorporated Research Institutions for Seismology (IRIS) and the GEOFON data center. The bulletin data were provided by the ISC and USGS/NEIC, and moment tensor solutions were obtained from the Global CMT Project. Figures were prepared using the GMT software package [*Wessel and Smith*, 1998].

References

Abelson, M., and A. Agnon (1997), Mechanics of oblique spreading and ridge segmentation, *Earth Planet Sci. Lett.*, *148*(3–4), 405–421, doi:10.1016/S0012-821X(97)00054-X.

Atwater, T., and K. C. Macdonald (1977), Are spreading centers perpendicular to their transform faults?, *Nature*, *270*(5639), 715–717, doi:10.1038/270715a0.

Ayele, A., D. Keir, C. Ebinger, T. J. Wright, G. W. Stuart, W. R. Buck, E. Jacques, G. Ogubazghi, and J. Sholan (2009), September 2005 mega-dike emplacement in the Manda-Harraro nascent oceanic rift (Afar depression), *Geophys. Res. Lett.*, *36*, L20306, doi:10.1029/2009GL039605.

Bergman, E. A., and S. C. Solomon (1990), Earthquake swarms on the Mid-Atlantic Ridge—Products of magmatism or extensional tectonics?, *J. Geophys. Res.*, *95*(B4), 4943–4965, doi:10.1029/JB095iB04p04943.

Bialas, R. W., and W. R. Buck (2009), How sediment promotes narrow rifting: Application to the Gulf of California, *Tectonics*, *28*, TC4014, doi:10.1029/2008TC002394.

Briggs, R. W., et al. (2006), Deformation and slip along the Sunda Megathrust in the great 2005 Nias-Simeulue earthquake, *Science*, *311*(5769), 1897–1901, doi:10.1126/science.1122602.

Buck, W. R., P. Einarsson, and B. Brandsdottir (2006), Tectonic stress and magma chamber size as controls on dike propagation: Constraints from the 1975–1984 Krafla rifting episode, *J. Geophys. Res.*, *111*, B12404, doi:10.1029/2005JB003879.

Cattin, R., N. Chamot-Rooke, M. Pubellier, A. Rabaute, M. Delescluse, C. Vigny, L. Fleitout, and P. Dubernet (2009), Stress change and effective friction coefficient along the Sumatra-Andaman-Sagaing fault system after the 26 December 2004 ($Mw = 9.2$) and the 28 March 2005 ($Mw = 8.7$) earthquakes, *Geochem. Geophy. Geosy.*, *10*, Q03011, doi:10.1029/2008GC002167.

Chamot-Rooke, N., C. Rangin, and C. Nielsen (2001), Timing and kinematics of Andaman basin opening, paper presented at AGU Spring Meeting, Abstract T42B-08.

Chlieh, M., et al. (2007), Coseismic slip and afterslip of the great *Mw* 9.15 Sumatra-Andaman earthquake of 2004, *Bull. Seismol. Soc. Am.*, *97*(1), S152–S173, doi:10.1785/0120050631.

Cochran, J. R. (2010), Morphology and tectonics of the Andaman Forearc, northeastern Indian Ocean, *Geophys. J. Int.*, *182*(2), 631–651, doi:10.1111/j.1365-246X.2010.04663.X.

Curray, J. R. (2005), Tectonics and history of the Andaman Sea region, *J. Asian Earth Sci.*, *25*(1), 187–228, doi:10.1016/j.jseaes.2004.09.001.

Curray, J. R., D. G. Moore, L. A. Lawver, F. J. Emmel, R. W. Raitt, M. Henry, and R. Kieckhefer (1979), Tectonics of the Andaman Sea and Burma, in *Geological and Geophysical Investigations of Continental Margins*, edited by J. Watkins, L. Montadert and P. W. Dickerson, pp. 189–198, Am. Assoc. Pet. Geol. Mem. 29, American Association of Petroleum Geologists, Tulsa, Okla.

Dick, H. J. B., J. Lin, and H. Schouten (2003), An ultraslow-spreading class of ocean ridge, *Nature*, *426*(6965), 405–412, doi:10.1038/nature02128.

Dziak, R. P., D. R. Bohnenstiehl, J. P. Cowen, E. T. Baker, K. H. Rubin, J. H. Haxel, and M. J. Fowler (2007), Rapid dike emplacement leads to eruptions and hydrothermal plume release during seafloor spreading events, *Geology*, *35*(7), 579–582, doi:10.1130/G23476A.1.

Dziak, R. P., D. R. Bohnenstiehl, H. Matsumoto, M. J. Fowler, J. H. Haxel, M. Tolstoy, and F. Waldhauser (2009), January 2006 seafloor-spreading event at 9 degrees 50′N, East Pacific Rise: Ridge dike intrusion and transform fault interactions from regional hydroacoustic data, *Geochem. Geophys. Geosyst.*, *10*, Q06T06, doi:10.1029/2009GC002388.

Eguchi, T., S. Uyeda, and T. Maki (1979), Seismotectonics and tectonic history of the Andaman Sea, *Tectonophysics*, *57*(1), 35–51, doi:10.1016/0040-1951(79)90100-8.

Einarsson, P., and B. Brandsdottir (1980), Seismological evidence for lateral magma intrusion during the July 1978 deflation of the Krafla volcano in Ne Iceland, *J. Geophys.*, *47*(1–3), 160–165.

Ekström, G. (1994), Anomalous earthquakes on volcano ring-fault structures, *Earth Planet. Sci. Lett.*, *128*, 707–712.

Engdahl, E. R., R. van der Hilst, and R. Buland (1998), Global teleseismic earthquake relocation with improved travel times and procedures for depth determination, *Bull. Seismol. Soc. Am.*, *88*(3), 722–743.

Engdahl, E. R., A. Villasenor, H. R. DeShon, and C. H. Thurber (2007), Teleseismic relocation and assessment of seismicity (1918–2005) in the region of the 2004 *Mw* 9.0 Sumatra-Andaman and 2005 *Mw* 8.6 Nias Island great earthquakes, *Bull. Seismol. Soc. Am.*, *97*(1), S43–S61, doi:10.1785/0120050614.

Escartin, J., D. K. Smith, J. Cann, H. Schouten, C. H. Langmuir, and S. Escrig (2008), Central role of detachment faults in accretion of slow-spreading oceanic lithosphere, *Nature*, *455*(7214), 790–795, doi:10.1038/nature07333.

Fitch, T. J. (1972), Plate convergence, transcurrent faults, and internal deformation adjacent to southeast Asia and western Pacific, *J. Geophys. Res.*, *77*(23), 4432–4460, doi:10.1029/JB077i023p04432.

Gahalaut, V. K., and K. Gahalaut (2007), Burma plate motion, *J. Geophys. Res.*, *112*(B10), B10402, doi:10.1029/2007JB004928.

Genrich, J. F., Y. Bock, R. McCaffrey, L. Prawirodirdjo, C. W. Stevens, S. S. O. Puntodewo, C. Subarya, and S. Wdowinski (2000), Distribution of slip at the northern Sumatran fault system, *J. Geophys. Res.*, *105*(B12), 28327–28341, doi:10.1029/2000JB900158.

Guzmán-Speziale, M., and J. F. Ni (1993), The opening of the Andaman Sea—Where is the short-term displacement being taken up?, *Geophys. Res. Lett.*, *20*(24), 2949–2952, doi:10.1029/93GL03053.

Helffrich, G. R. (1997), How good are routinely determined focal mechanisms? Empirical statistics based on a comparison of Harvard, USGS and ERI moment tensors, *Geophys. J. Int.*, *131*(3), 741–750, doi:10.1111/j.1365-246X.1997.tb06609.X.

Hey, R. N., H. W. Menard, T. M. Atwater, and D. W. Caress (1988), Changes in direction of seafloor spreading revisited, *J. Geophys. Res.*, *93*(B4), 2803–2811, doi:10.1029/JB093iB04p02803.

Hjörleifsdóttir, V., and G. Ekström (2010), Effects of three-dimensional Earth structure on CMT earthquake parameters, *Phys. Earth Planet. In.*, *179*(3–4), 178–190, doi:10.1016/j.pepi.2009.11.003.

Huang, P. Y., and S. C. Solomon (1988), Centroid depths of mid-ocean ridge earthquakes—Dependence on spreading rate, *J. Geophys. Res.*, *93*(B11), 13445–13477, doi:10.1029/JB093iB11p13445.

Kagan, Y. Y. (2003), Accuracy of modern global earthquake catalogs, *Phys. Earth Planet. In.*, *135*(2–3), 173–209, doi:10.1016/S0031-9201(02)00214-5.

Kamesh Raju, K. A., T. Ramprasad, P. S. Rao, B. R. Rao, and J. Varghese (2004), New insights into the tectonic evolution of the Andaman basin, northeast Indian Ocean, *Earth Planet Sci. Lett.*, *221*(1–4), 145–162, doi:10.1016/S0012-821X(04)00075-5.

Kamesh Raju, K. A., G. P. S. Murty, D. Amarnath, and M. L. M. Kumar (2007), The west Andaman fault and its influence on the aftershock pattern of the recent megathrust earthquakes in the Andaman-Sumatra region, *Geophys. Res. Lett.*, *34*(3), L03305, doi:10.1029/2006GL028730.

Kundu, B., D. Legrand, K. Gahalaut, V. K. Gahalaut, P. Mahesh, K. A. Kamesh Raju, J. K. Catherine, A. Ambikapthy, and R. K. Chadha (2012), The 2005 volcano-tectonic earthquake swarm in the Andaman Sea: Triggered by the 2004 great Sumatra-Andaman earthquake, *Tectonics*, *31*, TC5009, doi:10.1029/2012TC003138.

Lachenbruch, A. H. (1976), Dynamics of a passive spreading center, *J. Geophys. Res.*, *81*(11), 1883–1902, doi:10.1029/JB081i011p01883.

Lachenbruch, A. H., and G. A. Thompson (1972), Oceanic ridges and transform faults—Their intersection angles and resistance to plate motion, *Earth Planet Sci. Lett.*, *15*(2), 116–122, doi:10.1016/0012-821X(72)90051-9.

Lizarralde, D., et al. (2007), Variation in styles of rifting in the Gulf of California, *Nature*, *448*(7152), 466–469, doi:10.1038/nature06035.

Macdonald, K. C., D. S. Scheirer, and S. M. Carbotte (1991), Midocean ridges—Discontinuities, segments and giant cracks, *Science*, *253*(5023), 986–994, doi:10.1126/science.253.5023.986.

Maurin, T., F. Masson, C. Rangin, U. T. Min, and P. Collard (2010), First global positioning system results in northern Myanmar: Constant and localized slip rate along the Sagaing fault, *Geology*, *38*(7), 591–594, doi:10.1130/G30872.1.

McCaffrey, R. (1992), Oblique plate convergence, slip vectors, and forearc deformation, *J. Geophys. Res.*, *97*(B6), 8905–8915, doi:10.1029/92JB00483.

McCaffrey, R. (2009), The tectonic framework of the Sumatran subduction zone, *Annu. Rev. Earth Planet. Sci.*, *37*, 345–366, doi:10.1146/annurev.earth.031208.100212.

Menard, H. W., and T. Atwater (1968), Changes in direction of sea floor spreading, *Nature*, *219*(5153), 463–467, doi:10.1038/219463a0.

Mukhopadhyay, B., and S. Dasgupta (2008), Swarms in Andaman Sea, India—A seismotectonic analysis, *Acta Geophys.*, *56*(4), 1000–1014, doi:10.2478/s11600-008-0039-5.

Mutter, J. C., and J. A. Karson (1992), Structural processes at slow-spreading ridges, *Science*, *257*(5070), 627–634, doi:10.1126/science.257.5070.627.

Pesicek, J. D., C. H. Thurber, H. Zhang, H. R. DeShon, E. R. Engdahl, and S. Widiyantoro (2010), Teleseimic double-difference relocation of earthquakes along the Sumatra-Andaman subduction zone using a 3-D model, *J. Geophys. Res.*, *115*, B10303, doi:10.1029/2010JB007443.

Poupinet, G., W. L. Ellsworth, and J. Frechet (1984), Monitoring velocity variations in the crust using earthquake doublets—An application to the Calaveras Fault, California, *J. Geophys. Res.*, *89*(Nb7), 5719–5731, doi:10.1029/JB089iB07p05719.

Rangin, C., W. Maw, S. Lwin, W. Naing, C. Mouret, G. Bertrand, and GIAC scientific party (1999), Cenozoic pull apart basins in central Burma; the trace of the path of India along the western margin of Sundaland, paper presented at European Union of Geosciences conferences, Strasbourg, France.

Rodolfo, K. S. (1969), Bathymetry and marine geology of Andaman Basin, and tectonic implications for southeast Asia, *Geol. Soc. Amer. Bull.*, *80*(7), 1203–1230, doi:10.1130/0016-7606(1969)80[1203:BAMGOT]2.0.CO;2.

Roland, E., and J. J. McGuire (2009), Earthquake swarms on transform faults, *Geophys. J. Int.*, *178*, 1677–1690, doi:10.1111/j.1365-246X.2009.04214.X.

Rubin, A. M. (1992), Dike-induced faulting and graben subsidence in volcanic rift zones, *J. Geophys. Res.*, *97*(B2), 1839–1858, doi:10.1029/91JB02170.

Schaff, D. P., G. H. R. Bokelmann, W. L. Ellsworth, E. Zanzerkia, F. Waldhauser, and G. C. Beroza (2004), Optimizing correlation techniques for improved earthquake location, *Bull. Seismol. Soc. Am.*, *94*(2), 705–721, doi:10.1785/0120020238.

Seeber, L., M. H. Cormier, C. McHugh, O. Emre, A. Polonia, and C. Sorlien (2006), Rapid subsidence and sedimentation from oblique slip near a bend on the North Anatolian transform fault in the Marmara Sea, Turkey, *Geology*, *34*(11), 933–936, doi:10.1130/G22520A.1.

Sempere, J. C., G. M. Purdy, and H. Schouten (1990), Segmentation of the Mid-Atlantic Ridge between 24° N and 30° 40′N, *Nature*, *344*(6265), 427–431, doi:10.1038/344427a0.

Sevilgen, V., R. S. Stein, and F. F. Pollitz (2012), Stress imparted by the great 2004 Sumatra earthquake shut down transforms and activated rifts up to 400 km away in the Andaman Sea, *P. Natl. Acad. Sci. USA*, *109*(38), 15152–15156, doi:10.1073/pnas.1208799109.

Shuler, A., M. Nettles, and G. Ekström (2013), Global observation of vertical-CLVD earthquakes at active volcanoes, *J. Geophys. Res.*, *118*, doi:10.1029/2012JB009721.

Siebert, L., and T. Simkin (2002-). Volcanoes of the world: An illustrated catalog of Holocene volcanoes and their eruptions. *Smithsonian Institution*, *Global Volcanism Program Digital Information Series*, GVP-3, (http://www.volcano.si.edu/world/).

Sieh, K., and D. Natawidjaja (2000), Neotectonics of the Sumatran fault, Indonesia, *J. Geophys. Res.*, *105*, 28,295–228,326, doi:10.1029/2000JB900120.

Singh, S. C., J. McArdle, K. Johansen, and K. A. K. Raju (2010), Seismic images of the axial melt lens, Moho and deep penetrating faults at the sedimented Andaman Sea Spreading Center, paper presented at Fall Meeting, AGU, San Francisco, Calif., 13–17 Dec.

Smith, W. H. F., and D. T. Sandwell (1997), Global sea floor topography from satellite altimetry and ship depth soundings, *Science*, *277*(5334), 1956–1962, doi:10.1126/science.277.5334.1956.

Solomon, S. C., P. Y. Huang, and L. Meinke (1988), The seismic moment budget of slowly spreading ridges, *Nature*, *334*(6177), 58–60, doi:10.1038/334058a0.

Stein, R. S. (1999), The role of stress transfer in earthquake occurrence, *Nature*, *402*(6762), 605–609, doi:10.1038/45144.

Tanaka, A., and N. Fujii (1991), Energy-dissipation rates at ridge and transform-fault segments—A model of oblique spreading, *Geophys. Res. Lett.*, *18*(5), 857–860, doi:10.1029/91GL00996.

Taylor, B., K. Crook, and J. Sinton (1994), Extensional transform zones and oblique spreading centers, *J. Geophys. Res.*, *99*(B10), 19707–19718, doi:10.1029/94JB01662.

Thompson, G., and W. G. Melson (1972), Petrology of oceanic crust across fracture zones in Atlantic Ocean—Evidence of a new kind of sea-floor spreading, *J. Geol.*, *80*(5), 526–538, doi:10.1086/627779.

Tolstoy, M., D. R. Bohnenstiehl, M. H. Edwards, and G. J. Kurras (2001), Seismic character of volcanic activity at the ultraslow-spreading Gakkel Ridge, *Geology*, *29*(12), 1139–1142, doi:10.1130/0091-7613(2001)029<1139:SCOVAA>2.0.CO;2.

Tucholke, B. E., and J. Lin (1994), A geological model for the structure of ridge segments in slow-spreading ocean crust, *J. Geophys. Res.*, *99*(B6), 11937–11958, doi:10.1029/94JB00338.

Tuckwell, G. W., J. M. Bull, and D. J. Sanderson (1996), Models of fracture orientation at oblique spreading centres, *J. Geol. Soc. London*, *153*, 185–189, doi:10.1144/gsjgs.153.2.0185.

Uyeda, S., and H. Kanamori (1979), Back-arc opening and the mode of subduction, *J. Geophys. Res.*, *84*(Nb3), 1049–1061, doi:10.1029/JB084iB03p01049.

Vigny, C., A. Socquet, C. Rangin, N. Chamotrooke, M. Pubellier, M. N. Bouin, G. Bertrand, and M. Becker (2003), Present-day crustal deformation around Sagaing fault, Myanmar, *J. Geophys. Res.*, *108*(B11), 2533, doi:10.1029/2002JB001999.

Waldhauser, F. (2009), Near-real-time double-difference event location using long-term seismic archives, with application to Northern California, *Bull. Seismol. Soc. Am.*, *99*(5), 2736–2748, doi:10.1785/0120080294.

Waldhauser, F., and W. L. Ellsworth (2000), A double-difference earthquake location algorithm: Method and application to the northern Hayward fault, California, *Bull. Seismol. Soc. Am.*, *90*(6), 1353–1368, doi:10.1785/0120000006.

Waldhauser, F., and D. Schaff (2007), Regional and teleseismic double-difference earthquake relocation using waveform cross-correlation and global bulletin data, *J. Geophys. Res.*, *112*, B12301, doi:10.1029/2007JB004938.

Waldhauser, F., D. P. Schaff, T. Diehl, and E. R. Engdahl (2012), Splay faults imaged by fluid-driven aftershocks of the 2004 *Mw* 9.2 Sumatra-Andaman earthquake, *Geology*, *40*(3), 243–246, doi:10.1130/G32420.1.

Walter, T. R., and F. Amelung (2007), Volcanic eruptions following $M \geq 9$ megathrust earthquakes: Implications for the Sumatra-Andaman volcanoes, *Geology*, *35*, 539–542, doi:10.1130/G23429A.1.

Wessel, P., and W. H. F. Smith (1998), New, improved version of the Generic Mapping Tools released, *EOS, Trans. Am. Geophys. Un.*, *79*, 579, doi:10.1029/98EO00426.

Widiyantoro, S., and R. van der Hilst (1997), Mantle structure beneath Indonesia inferred from high-resolution tomographic imaging, *Geophys. J. Int.*, *130*(1), 167–182, doi:10.1111/j.1365-246X.1997.tb00996.X.